PHD THESIS

UNIVERSITÀ DEGLI STUDI DI NAPOLI "FEDERICO II"

DIPARTIMENTO DI INFORMATICA E SISTEMISTICA

DOTTORATO DI RICERCA IN INGEGNERIA
INFORMATICA ED AUTOMATICA

INNOVATIVE MEASUREMENT METHODS FOR HOMELAND SECURITY APPLICATIONS

MARCELLO ASCIONE

Coordinatore del corso di Dottorato
Ch.mo Prof. Francesco GAROFALO

Tutori
Ch.mo Prof. Leopoldo ANGRISANI
Dott. Ing. Michele D'URSO
Dott. Ing. Aniello BUONANNO

A.A. 2011-2012

Contents

List of Figures

LIST OF FIGURES

List of Tables

Acronyms

USAR, Urban Search and Rescue

MUSIC, Multiple Signal Classification

TWS, Through Wall Sensing

TWI, Through-Wall Imaging

BP, back projection

UWB, Ultra Wideband

TM-UWB, Time-Modulated UWB

CS, Compressive Sensing

RPMI, Random Modulation pre-Integration

TWRI, Through Wall Radar Imaging

NDOF, Number of Degrees of Freedom

LO, Local Oscillator

SVD, Singular Value Decomposition

FFT, Fast Fourier Transform

SNR, Signal-to-Noise Ratio

TWR, Through Wall Radar

VSD, Vital Sign Detector

STTW, Sense-Through-The-Wall

GSSI, Geophysical Survey Systems, Inc.

TB-model, Target-Based model

TSVD, Truncated Singular Value Decomposition

MS, Measurement System

SF-CW, Stepped Frequency Continuous Wave

PEC, Perfect Electrical Conductor

FDTD, Finite-Difference Time-Domain

MTI, Moving Target Indicator

CW, Continuous-Wave

FIR, Finite Impulse Response

AIC, Aikake's Information Criterion

ITC, Information Theoretical Criteria

DR, Dynamic Range

ABC, Absorbing Boundary Condition

RMSE, Root Mean Square Error

AWGN, Additive White Gaussian Noise

DFT, Discrete time Fourier Transform

DA, Amplitude Displacement

OI, Observation Interval

LNA, Low Noise Amplifier (LNA)

Introduction

In recent years, the demand for security applications has lead to improvements in the effectiveness of safety operations in dangerous situations and to the development of methods for obtaining information about the internal features of rooms or structures, as well as the location of any people present therein [1].

The ability to ‘see’ inside not accessible regions by using electromagnetic waves is an issue of strong interest in several applications in the homeland protection field. The complexity of the scenario of interest is such to claim for the development of new architectural and technological solutions useful also for the modern radar sensors. Compensation for multi-path, dispersion, and reflection requires a detailed knowledge of the electromagnetic interactions between the different parts of the investigated scenario.

An imaging architecture must address the physical propagation effects and proper modeling of the environment so that the sensor can sense deeper within the buildings. Sensor architectures must support system design decisions to resolve significant building parameters but are not overly sensitive to microstructure (such as cavities in concrete block) that are less important to operational tasks.

This may also require fast propagation solvers to work through 3-D models, and fast processing architectures that can handle these tasks in near-real-time. Frequency choices must strike careful balances between wall attenuation favoring lower frequencies and resolution favoring higher frequencies. Lower frequencies also have the potential benefit that smaller microstructure (wiring, pipes, air gaps in concrete block walls, etc.) may provide less distortion on the Radio Frequency signal.

All of this must be factored into the propagation assessment and physical modeling. Starting from these considerations, there is the need for developing new procedures and systems able to extract information from heterogeneous scenario to allow and simplify complex decisions.

This work deals with the implementation of a suitable technological support to improve the success likelihood of Urban Search and Rescue (USAR) missions.

Here we introduce a new architectural solution to detect and track humans beyond walls for homeland protection applications. Two different measurement methods have been developed, the first one for detection and tracking of moving targets in two-dimensional scenes exploiting an advanced imaging technique, which takes advantages from a regularized linear inversion scheme. The second method has been developed for life signs detection and it takes advantage from a suitable spatial smoothing strategy applied to the traditional algorithm for Multiple Signal Classification (MUSIC), mandated to single out the spectral components of the received signal.

A description of the issues related to the detection of moving targets and vital signs and an overview of existing solutions in terms of processing techniques and products on the market will be presented. In the second chapter the functional architecture of the proposed system for Through Wall Sensing (TWS) will be described. In following chapters the dissertation is focused on development of measurement methods for tracking of moving target and vital signs detection. In Chapter 5 the analysis of numerical results is performed in order to verify the behavior of proposed measurement methods in presence of noise. In the last Chapter the achieved results in the experiments and the adopted instrumentation will be presented and discussed.

Chapter 1

Fundamentals

The goal of this chapter is to provide the key concepts necessary to fully understand the content of this dissertation. The first section introduces the basic issues about Through Wall Sensing, a typical inverse problem. In the second section an overview of most important products on the market is presented.

1.1. Through Wall Sensing

TWS is the capability of determine if someone is in a room before putting themselves in harm's way and to save lives by using motion and images to differentiate between a hostage and a hostage-taker [2]. It can also detect motion through floors and rubble following a building structure failure and, therefore, help in the search for survivors. It allows users to conduct room-to-room searches for suspected terrorists, map the interior of buildings, and find military combatants and weapons caches all through an interior or exterior building wall.

Through the Wall Surveillance technologies do not even need to be placed against a wall and can be used to perform standoff searches, for example, from a vehicle into a building.

We consider through wall sensing from two points of view:

- To determine the presence of moving people in a room or building without entering this space due to some dangerous conditions (e.g. fire or armed persons).
- To detect static people beyond the wall or buried under rubble after an earthquake.

Radiofrequency imaging can prove effective in detecting and monitoring the presence of human subjects from a distance and through barriers, such as walls [3]-[8]. To this aim, two main conditions have to be satisfied. Depending on the electromagnetic properties of the wall, a suitable trade-off between the desired resolution of hidden objects and the permeability of the structure to the used electromagnetic radiation has to be found out. Moreover, the adopted reconstruction algorithms, designed to provide an image of the scene including any moving target of interest, have to operate on the acquired data in a reasonable computational time, which is a fundamental prerequisite to succeed in real time tracking the position of the targets.

The detection of static people is based on the Doppler theory, and assumes that, when a human body is exposed to a continuous wave microwave source, the reflected signal turns out in a phase-modulated one, which is essentially related to the (periodic) chest movement caused by respiration and heartbeat. So, vital signs can be detected from the reflected waves by adopting a suitable demodulation scheme.

1.1.1. Inverse problems

In this subsection the definition of inverse problem is provided as reported in [9]. From the point of view of a mathematician the concept of an inverse problem has a certain degree of ambiguity which is well illustrated by a frequently quoted statement of J.B. Keller [10]: ‘We call two problems *inverses* of one another if the

formulation of each involves all or part of the solution of the other. Often, for historical reasons, one of the two problems has been studied extensively for some time, while the other has never been studied and is not so well understood. In such cases, the former is called the *direct problem*, while the latter is the *inverse problem*'.

In any domain of mathematical physics one finds problems satisfying the requirements stated by Keller. In general these problems are related by a sort of duality in the sense that one problem can be obtained from the other by exchanging the role of the data and that of unknowns: the data of one problem are the unknowns of the other and conversely. As a consequence of this duality it may seem arbitrary to decide what is the direct and what is the inverse problem.

In classical mechanics a direct problem is, for instance, the computation of the trajectories of particles from knowledge of the forces. Then the inverse problem is the determination of the forces from knowledge of the trajectories. From this point of view Newton not only stated the basic laws of mechanics, and therefore the basic equations of the direct problem, but also solved the first inverse problem when he determined the gravitation force from the Kepler laws describing the trajectories of the planets.

Other examples, however, are more appropriate for the modern applications of inverse methods. In scattering and diffraction theory, the direct problem is the computation of the scattered (or diffracted) waves from the knowledge of the sources and obstacles, while the inverse problem consists of the determination of the obstacles from the knowledge of the sources and of the scattered waves. Inverse problems of this kind are fundamental for various methods of non-destructive evaluation (including medical imaging) which consist of sounding an object by means of a suitable radiation source.

Another example of a direct problem in wave-propagation theory is the computation of the field radiated by a given source, for instance the radiation

pattern of a given antenna; then the inverse problem is the determination of the source from knowledge of the radiated field.

Other examples come from instrumental physics, i.e. the physics of instruments such as electronic devices, imaging systems, etc. Here the direct problem is the computation of the output of instrument (the image) being given the input (the object) and the characteristics of the instrument (impulse response function, etc). Then the inverse problem is the identification of the input of a given instrument from the knowledge of the output.

Finally a direct problem is a problem oriented along a cause-effect sequence; it is also a problem directed towards a loss of information: its solution defines a transition from a physical quantity whit a certain information content to another quantity with a smaller information content. This property is common to most direct problems. In general it implies that the solution is much smoother than the data: the image provided by a band-limited system is smoother than the corresponding, the scattered wave due to an obstacle is smooth even if the obstacle is rough, and so on.

1.1.2. Through Wall Imaging

Through Wall Imaging (TWI) consists in imaging hidden objects using electromagnetic waves. This problem is of great interest as the aim of detecting and localizing hidden objects is shared in many applicative contexts, both military and civilian, as shown in Fig.1, examples of which are security, peace keeping, law enforcement operations, or even searches for suspects and hostages [11]–[14].

In order to ensure the success of TWI, different conditions have to be met. First, the illuminating radiation must be able to pass through the obstacle with “relatively little” attenuation and, at the same time, to achieve the “reconstruction” of the hidden object with good resolution. This entails, depending on the

electromagnetic properties of the wall, the necessity of exploiting frequency bands ranging between a few hundred MHz and 2–3 GHz [15].

Second, the other important requirement regards the development of "reliable" reconstruction algorithms (in the sense that one should be able to foresee what is expected to be retrieved) working in a "reasonable" computational time.

Figure 1: TWI - Applicative scenarios

Several works concerning through-the-wall detection of targets have been presented [16]-[24]. Even though they certainly meet the trade-off condition between the desired resolution and the permeability of the structure, some of them shows results, either numerical or experimental, based only on non real-time measurements methods and achieved in very controlled environments.

As an example, the method proposed in [16] exploits the subtraction of successive frames of the cross-correlation signals between each received element signal and the transmitted signal to isolate moving targets in heavy clutter. Images of moving targets are subsequently obtained using the back projection (BP) algorithm. The method takes about 4 hours on a personal computer operating at a clock frequency of 2.4 GHz to generate each data frame in simulated experiments, thus preventing its use for real time security applications. Furthermore the method assumes that the wall characteristics are known exactly, but in real operation, the wall parameters are not known a priori. When the assumed wall parameters are incorrect, the image of the moving target is displaced.

Besides traditional synthetic aperture radars, several examples of fixed aperture imaging systems have also been proposed. Such systems are, however, heavy, large and expensive, and their operations are based on Vivaldi or horn type antennas (i.e. not easily portable), thus making their use in limited spaces, such as a room or a building very difficult [17].

Ultra Wideband (UWB) is a promising technology for high resolution radars, collision detectors, high data rate communication systems and geolocation devices. The narrow pulse width allows the use of UWB signals in accurate positioning and high-resolution imaging applications [18]. As a consequence, they are usually proposed and adopted in sensors for subsurface imaging applications, due to their capability of penetrating sand providing good measurement resolution [19].

Thanks to the availability of UWB technology, time-modulated UWB (TM-UWB) radars have become even more adopted for through-the-wall imaging applications [20]. It is worth noting that, due to the presence of spurious spectral lines, conventional TM-UWB radars fail to achieve the ideal resolution and detection performance [21]. Recently, some research activities have been focused on noise UWB radars [22], since they achieve better resolution performance than previous TM-UWB radars and grant robust detection in several operating conditions. However, as for all the devices based on a radar approach, they suffer from a stringent requirement in terms of coherent reception at the receiver; assuring coherence over a wide bandwidth results to be not only challenging but also impossible when the transmitter and receiver are physically separated by a distance [23]. Moreover, bi-static and multi-static configurations (usually adopted to improve the coverage performance and assure a distortion free synchronization) become difficult to put in practice for through-the-wall imaging applications.

Finally, a problem always associated with through-the-wall systems operating in the frequency range from 1 GHz to 10 GHz is the ubiquitous presence of room reverberations. Their origin relies on multiple reflections of the transmitted signal

by the walls, causing numerous false alarms associated with weak targets (i.e. targets whose backscattered signals exhibit low amplitude).

In [24], a compact UWB radar system for indoor and through-the-wall ranging and tracking of moving objects has been built up by using the compact self-grounded Bow-Tie antennas and the low-cost Novelda transceiver. Robust and accurate algorithms for ranging and tracking have been developed. The most attractive aspect of the system is its low-cost and compact size. However, due to its small size, the dynamic range is relatively low, and therefore, only short-range applications are feasible.

Recently, a new framework for simultaneous sensing and compression, referred to as compressive sensing (CS), has received considerable attention and has been successfully applied in many fields, such as signal/image processing, communications, geophysics, remote sensing and radar imaging [25]-[27]. In [25], through-the-wall imaging by means of impulse radar has been faced within the framework of compressive sensing. Rather than sampling the time-domain signal at or above the Nyquist rate, the random modulation pre-integration (RMPI) architecture has been employed for CS projection measurement, and has led to significant data reduction. Target space sparsity has been exploited to solve the TWI problem using sparse constraint optimization. Numerical imaging results of point-like and spatially extended targets have clearly shown the advantages of using CS in urban sensing applications.

In [26], a compressive-sensing-based through-the-wall imaging algorithm has been presented. Preliminary numerical results have been given regarding relevant issues such as required number of measurements for a given sparsity level, measurement strategy to subsample in the frequency and space domains and imaging performance for different noise levels. Simulations with off-the-grid targets and unknown parameters have been performed, and it has been observed that for small grid sizes or errors in the unknown parameters, the imaging

performance is not severely affected, whilst large grid sizes or errors degrade the reconstructed image.

In [27], a sparse tomographic inverse scattering approach for fast data acquisition and 3-D scene reconstruction in Through Wall Radar Imaging (TWRI) applications has been dealt with. While a combined 2-D sliced approach has been used for 3-D scene representation, the number of degrees of freedom (NDOF) of the scattered field has been exploited in order to choose the number of needed non-redundant spatial measurements. The performance of the proposed scheme has been assessed using experimental data collected from 3-D scattering scenes in a semi-controlled environment. The results have shown that use of a limited number of measurement aperture points, as predicted by the NDOF analysis, reduces the data acquisition time and permits to achieve an image quality comparable with that obtained by using a finer grid of spatial measurements.

1.1.3. Life Signs Detection

The detection of life signs, such as breathing and/or heartbeat, is nowadays becoming a fundamental topic in urban search and rescue strategies, Fig.2.

Microwave signals have been exploited in the past for detecting people trapped under rubble or behind concrete wall, as discussed in [28]-[31]. In particular, Doppler radar systems can be applied to detect vital signs like respiration and heartbeat.

The human phenomena of interest are:

- **Heart rate**: The number of heart beats per unit time, usually per minute. The typical resting heart rate in adults is 60-90 bpm [32].
- **Breathing** frequency is the number of breaths taken within a set amount of time, typically 60 seconds. During quiet breathing at rest, an adult's breathing rate averages 12 breaths per minute [33].

Figure 2: USaR applications

In [28] a sensitive life-detection system using microwave radiation for locating human subjects buried under earthquake rubble or hidden behind various barriers is shown. This system operating at 1150 or 450 MHz can detect the breathing and heartbeat signals of human subjects through an earthquake rubble or a construction barrier of about 10-ft thickness. This system has been tested extensively with satisfactory results in simulated earthquake rubble constructed at the Electromagnetics Laboratory of Michigan State University. It has also been tested in a field test using realistic earthquake rubble at Rockville, MD, conducted by Maryland Task Force of FEMA.

The choice of these operating frequencies is related to the considerations about the penetrability of earthquake rubble or collapsed building debris, so the frequency of the electromagnetic wave need to be in the L or S band.

However, the adopted clutter cancellation procedure requires measurements on stationary background, i.e. in absence of target. In operating conditions is not possible to know this amount in a deterministic manner, further the proposed processing does not take into account the problem of null points described in [36] and leakage because the imperfection of the circulator [38]. A sophisticated signal processing scheme may further improve the system performance to eliminate the effects of the background noise created by the environment and operators.

In [29] direct-conversion microwave Doppler-radar transceivers have been fully integrated in 0.25μm silicon CMOS and BiCMOS technologies. These chips operate at 1.6 and 2.4 GHz, each with a single oscillator and output power comparable to the low-end power of consumer electronics (under 10 mW). They have detected movement due to heartbeat and respiration 50 cm from the subject and in free space condition, which may be useful in infant and adult apnea monitoring. A quadrature (I/Q) receiver is taken into account in order to avoid null points. The paper describes an interesting characterization of the residual phase noise, which is a limiting factor in proposed system, depends on both the target range and oscillator phase noise. In fact when the same source is used for transmitting and receiving, the phase noise of the received signal is correlated with that of the local oscillator (LO), with the level of correlation dependent on the time delay between the two signals. When the delay is small, this effect greatly decreases the noise spectrum at baseband. For example, at a 50-cm range, the baseband noise at 10 Hz is 134 dB below the RF phase noise. In a radar application, this time delay is proportional to the target range. The adopted processing is very simple and provides a standard filtering in the band of interest of the received signal in free space. In fact the authors declare that a more advanced signal processing and further system integration is necessary.

An interesting system based on double-sideband transmission in Ka-band is proposed in [30]-[31]; its main advantages are related to the operating frequency of the adopted sensors, the short wavelength of which assures higher sensitivity to the limited chest-wall movements with respect to other solutions exploiting signals characterized by a lower frequency value. However, the considered Ka-band strongly limits its applicability, due to the low penetration capability. The heartbeat signal was first separated from the respiration signal by a Butterworth BPF with passband from 0.7 to 3 Hz. The filtered signal was then windowed and auto-correlated. After that, a Fast Fourier Transform (FFT) was applied to the auto-correlated signal to obtain the heartbeat rate.

An interesting solution for detecting life signs in free space and/or behind concrete walls has recently been proposed in [34]. It relies on a simple scattering model and uses a measurement configuration working in X-band. In particular, a suitable compensation of the undesired signals associated with stationary objects is carried out, and a proper frequency domain, correlation based signal processing algorithm is applied to assure very high detection sensitivity. The unknown principal Doppler frequency is determined as the quantity that maximizes the scalar product between the square modulus of the Fourier transform of measured signal and the square modulus of the Fourier transform of the model signal.

The technique based on maximum correlation has limitations in terms of signal to noise ratio compared to more sophisticated techniques in terms of noise rejection (MUSIC, SVD, etc).

The effective use of all these systems is limited by the complexity of some scenarios of interest, which requires high performance in terms of signal-to-noise ratio (SNR) robustness and resolution. These requirements can be met by either enhancing the hardware sensitivity or developing more efficient processing techniques.

One of the most important issues related to the detection of vital signs is the problem of null points in the received signal. When the subject is located at a certain distance from the antenna, in fact, it can happen that the reflection appears so attenuated as to have a total loss of information concerning the cardiopulmonary rhythms. The null-point problem is more severe for higher frequency operation. In [35], a band radio system that detects human heartbeat and breathing signals using low-power double-sideband transmission has been introduced. The paper described the theory and implementation of the frequency-tuning technique and double-sideband transmission to avoid null points and improve system performance. The short wavelength at the band increases the sensitivity of phase shift due to small displacement and therefore improves the signal-to-noise ratio and detection distance. The use of double-sideband

transmission helps resolve the null-point problem and improves the detection reliability. A frequency-tuning technique is applied to switch a null point to an optimum point, resulting in almost doubling the detection accuracy.

Another relevant issue is the presence of static clutter related both to the surrounding environment and the fixed parts of the human body. Suitable signal processing techniques could strongly attenuate this kind of noise to assure more reliable detection [36]. In mentioned paper is shown the performance of the complex signal demodulation and the arctangent demodulation for random body movement cancellation in Doppler radar vital sign detection. If the dc offset of the baseband signal is accurately calibrated, both demodulation techniques can be used for random body movement cancellation. While the complex signal demodulation is less likely to be affected by a dc offset, the arctangent demodulation has the advantage of eliminating harmonic and intermodulation interference at high carrier frequencies. When the dc offset cannot be accurately calibrated, the complex signal demodulation is better.

In many implemented system schemes, the adopted hardware can introduce an undesired component related to the non-ideality of some component, such as a circulator [37]. This component is known as leakage. A leaking signal should be taken into account in the received signal model, it is represented as a dc-offset component in addition to the useful signal.

In [38], a harmonic analysis highlighting the effects of non-linear cosine transfer function in non-contact vital sign detection is shown. Harmonics and intermodulation effects have been both theoretically analyzed and proved through simulations and actual measurements. In particular, the intermodulation effects represent a relevant limit to heartbeat detection, since it proves to be more error prone with respect to breathing detection. It has been shown that in contrast to the common sense that detection accuracy can always be increased by increasing the carrier frequency, there is an optimum choice of carrier frequency. At the optimum carrier frequency, the heartbeat signal component can be maximized in

the premise that the harmonics interference and the intermodulation interference are not so large as to affect the detection accuracy.

In [39] an integrated solution based on a heterogeneous network of highly specialized sensors for through-the-wall applications in complex scenario like buildings has been introduced. The network mainly consists of two kinds of sensors: a Through the Wall Radar (TWR), addressed to the detection and tracking of moving targets, and a Vital Signs Detector (VSD), capable of assessing the presence of standing and living people. With specific regard to the VSD, a measurement method for vital signs detection is proposed. The method takes advantage of a traditional quadrature demodulation scheme as well as MUSIC algorithm to detect life signs behind walls. In particular, demodulation technique allows removing the DC component related to static clutter and extracting the useful signal also in correspondence with null points, as shown in [38]. The paper is focused on the breathing detection because the contemporary detection of breath and beat is more complex for the presence of intermodulation products. Therefore it is necessary adequate decorrelation procedure to separate the frequency components present in the received signal.

1.2. Analysis of existing sensors

In this section a description of existing sensors available on the market is provided: PRISM 200, Xaver™ 400 and LifeLocator® III.

PRISM 200 is a product of the Defense & Security Campaign at Cambridge Consultants, while Xaver™ 400 is manufactured by Camero, which is a world leading provider and pioneer of Sense-Through-The-Wall (STTW) solutions. Finally LifeLocator® III is made by Geophysical Survey Systems, Inc. (GSSI) . The LifeLocator® system uses UWB radar technology to improve the odds of recovering living victims of avalanches, flash floods, earthquakes, building collapses and other man-made disasters.

1.2.1. PRISM 200

PRISM 200[1] is a lightweight, durable and highly sophisticated through-wall radar, Fig.3. It is designed to provide police, special forces and the emergency services with accurate covert intelligence of the location and movement of people in situations where it would otherwise be impossible to gain such insight.

Figure 3: PRISM 200

Using ultra-wide band radar, Prism 200 provides a 3D view through brick, block and concrete walls, and doors, and over a range of up to 20 meters, providing comprehensive coverage of internal spaces. It can be used for the rapid evaluation of room occupancy or it can be used for more detailed intelligence gathering. It is currently deployed in over 40 countries around the world.

The product allows to track the movement of objects or people through walls (but does not allow the discrimination between objects and human being). PRISM 200 is a compact sensor, working in 1.6–2.2 GHz band. It does not allow the detection of people by using their life signs, and does not take into account the internal layout, so that false detections could be frequent. The limited antenna

[1] http://www.cambridgeconsultants.com

array size drastically affects the cross range resolution. Table I summarizes the technical specifications of the system PRISM 200.

TABLE I: PRISM 200 - TECHNICAL SPECIFICATION

	PRISM 200
Device Type	Through-Wall Radar
Detection capacity	Still and moving targets
Detection Range	Up to 20 m
Angular Coverage	120° in azimuth 90° in elevation
Display	2D and 3D colour display resolution 640×480
Wall materials	Bricks, wood, cinder blocks, cement, reinforced concrete.
Bandwidth	[1.6 – 2.2] GHz
Resolution	30 cm
Size and weight	(305×450×210) mm; 5.7 Kg battery included
Battery duration	4.5 hours, continuous use; 24 hours standby
Environment	Rough, working temperature -20°C - 55°C
Transmitted Power	-10 dBm averaged on the bandwidth

1.2.2. Camero Xaver™ 400

The Xaver™ 400[2] allows for quick location of people hidden by walls and barriers, enabling tactical teams to step into the known and obtain mission-critical information, Fig.4. The Xaver™ 400 is a compact, lightweight and durable

[2] http://www.camero-tech.com

personal device, optimized for the speed of tactical entries. It gives special ops and rescue forces critical information in real-time about the number of people and their location behind a wall. Simple to operate, the Xaver™ 400 provides vital information when and where it is needed.

Figure 4: Xaver™ 400

Xaver™ 400 allows to track the movement of objects or people trough walls (but does not allow the discrimination between objects and human being; it is more compact and lighter than the previous one, it works in 3–10 GHz band. Like the previous one, this sensor does not allow the detection of people by using their life signs, and does not take into account the internal layout, so that false detections could be frequent. The operative frequencies could be too high to ensure an adequate penetration in high loss wall. Finally Table II provides the specifications of the described radar.

TABLE II:CAMERO XAVER 400- TECHNICAL SPECIFICATION

	CAMERO XAVER 400
Device Type	Through-Wall Radar

Detection capacity	Still and moving targets
Detection Range	4m, 8m, 20m
Angular Coverage	80° in azimuth and in elevation
Display	2D in the view plane
Wall materials	Chalk, bricks, cement, reinforced concrete, plastering, drywall.
Bandwidth	[3 – 10] GHz
Resolution	Less than 1 m
Size and weight	(370×225×120) mm; 2.95 Kg battery included
Battery duration	Rechargeable: 2.5 hours Primary batteries: 4.5 hours
Environment	-
Transmitted Power	-
Power supply	Rechargeable and primary batteries
Wireless video	Transmitter video wireless, coverage up to 100m

1.2.3. LifeLocator® III

The LifeLocator[3] is a compact, standalone, UWB trapped-victim-detection radar, Fig.5. It exploits UWB technology to greatly improve the odds of rescue following structural collapses due to weather, fire or catastrophic attack, avalanches, flash floods, earthquakes or other natural disasters. The LifeLocator® is ideally suited for life rescue, locating victims by sensing even the minor movements of shallow breathing. The sensor detects signals that are relayed in real-time to a PDA. The information allows rescue personnel to accurately and rapidly determine the distance to the victim. A key advantage of the technology is

[3] http://www.gssilifelocator.com/

that it is not misled by scent drift or from the scent of the deceased. It does not require line of sight or the complete silence that challenges video and audio monitoring search and rescue tools. Ease of mobility and placement over treacherous ground further enhances the system's in-field effectiveness.

Figure 5: LifeLocator® III (Not to scale)

LifeLocator® is capable of detecting fractions of motions (i.e. those associated with extremely shallow respiratory) in such a way that even the most injured victim of any natural or man-made disaster, which can trap living beings, can be located. The maximum depth of respiratory detection is 4.5 m. Table III provides the specifications of the system.

TABLE III: LIFELOCATOR® III - TECHNICAL SPECIFICATION

	LifeLocator® III
Device Type	UWB radar
Motion Detection	Up to 30 ft (10 m)
Breathing Detection	Up to 18 ft (6 m)

Detection Volume	4500 cubic ft (127 cubic m)/3 minutes
Wireless range	up to 150 ft (30 m) Wi-Fi
Sensor Unit	
Size and weight	18×18×9 in (45×45×22 cm); 21 lbs (9 kg)
Battery life	up to 6 hours
Battery type	Li-ON
PDA control unit	
Size and weight	3.75×6.5 in (9.5×16.5 cm); 17 oz (490 g)
Battery life	up to 10 hours

Chapter 2

Architectural Solution

In the previous Chapter the importance of Through Wall Sensing in the Homeland Security applications has been highlighted. This chapter describes the developed architectural solution for the detection and tracking beyond wall of moving and static people.

In the first section a high-level description of the developed functional architecture is provided. In following sections the implementation of introduced functions is described and discussed. In particular the proposed innovative measurement methods to extract useful information for target detection are only introduced while a detailed description will be presented in the following Chapters.

2.1. Functional Architecture

The developed architectural solution is characterized by innovative signal processing paradigms and advanced systems for:

- solving complex electromagnetic scattering problems;
- tracking humans inside of buildings;
- detecting life signs beyond obstacles;
- estimating the internal layout of the building and electromagnetic parameters of the wall;

- combining all information in an exciting interplay between electromagnetic propagation, signal processing, and knowledge-based reasoning approach.

The proposed system architecture is able to detect the vital signs, to estimate the thickness and electromagnetic parameters of the wall, to estimate the internal building layout, and to track the movement of persons inside buildings by processing the electromagnetic field measured from the outside of the buildings (i.e. the signal coming from the investigated area and measured by the received antennas).

A (quasi) real time procedure to estimate the internal layout of the building has been developed. The estimated building layout and electromagnetic parameters of the wall is then exploited to obtain the model of scenario and localize and tracking individuals inside the building. The innovative procedures developed to a priori estimate the internal building layouts are a key point of the proposed system architecture and also the main differences between the proposed one and the existing. For the implementation of all these functionalities an innovative electromagnetic scattering model has been developed. In Fig.6 the overall functional architecture is shown.

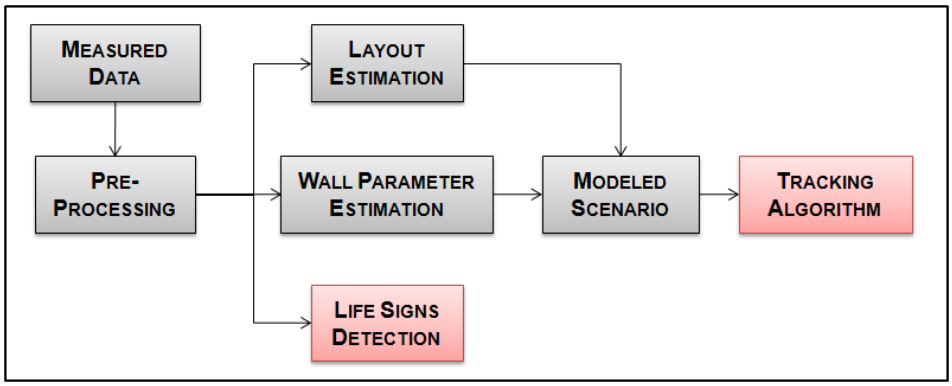

Figure 6: Functional Architecture

2.2. Wall Parameters Estimation

The aim of this block is to estimate the thickness and the electromagnetic parameters of the wall [40]. The estimation procedure takes advantage from the circumstance that the shape and the amplitude of the "first part" of the measured signal (in time domain) only depend on these parameters. The system will be equipped with a database storing signals for opportune values of the thickness and dielectric constant. These signals have been synthetically computed via a full-wave electromagnetic model, including a 3D representation of both wall and antennas.

The wall parameters are estimated by minimizing the following functional:

$$\Phi(\varepsilon_r, d) = \int_0^{T(\varepsilon_r,d)} \left[D(\varepsilon_r, d, t) - M(t) \right]^2 dt \tag{2.1}$$

where $D(\varepsilon_r, d, t)$ are the signals calculated for opportune values of the couple (ε_r, d), while $M(t)$ is the measured signal. This functional represents the mismatch between the measured signal and the database signals. Finally the wall parameters are obtained by following minimization

$$\left(\tilde{\varepsilon}_r, \tilde{d}\right) = \min_{(\varepsilon_r, d)} \left\{ \Phi(\varepsilon_r, d) \right\} \tag{2.2}$$

In particular the time portion of interest is chosen so that the contributions due to the scattering objects located beyond the wall are mainly concentrated outside this interval. This capability is the first step for the reconstruction of the internal building layout. The more accurate is the wall parameters estimation the more accurate will be the retrieved layout.

2.3. Layout Estimation

Several approaches have been increasingly documented in the literature showing abilities to sense beyond a single wall. But shadowing, attenuation, multipath, refraction, diffraction, and dispersion affect the propagation of the electromagnetic waves beyond the first interface. Then, it is crucial to determine the layout of investigated structure, where persons may be, and even identify objects within structure.

In this functional block "layout estimation" a model-based representation (a detailed description of model-based representation is provided in the following chapter), that best matches the collected data, using a full-wave propagation model, allow to retrieve the geometrical features of the investigated structure, Fig.7.

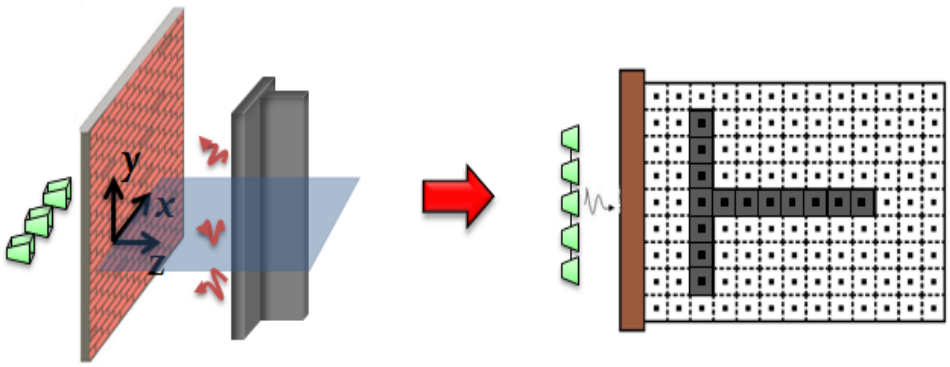

Figure 7: Model based representation for layout estimation

The common approaches usually neglect propagation distortions such as those encountered by electromagnetic waves propagating through walls and objects. These distortions degrade the accuracy and can lead to ambiguities in detection, localization and tracking of the moving targets.

2.4. Modeled Scenario

The aim of this section is to estimate the electromagnetic response of the scenario reconstructed thanks to the Wall Parameters Estimation and Layout

Estimation. In particular, once the overall geometrical characteristics of the room are known it is possible to numerically evaluate the Green's function of the investigated region under the hypothesis that the electromagnetic properties of each wall are the same of the estimated one. An accurate evaluation of the scenario's electromagnetic response is important for taking into account the scattering phenomena due to the interaction of the electromagnetic waves with the environment such as diffraction and multipath. This processing block allows to compensate the defocusing and the delocalization of the targets due to the presence of the wall and the layout. An example of scenario reconstruction is provided in Fig.8.

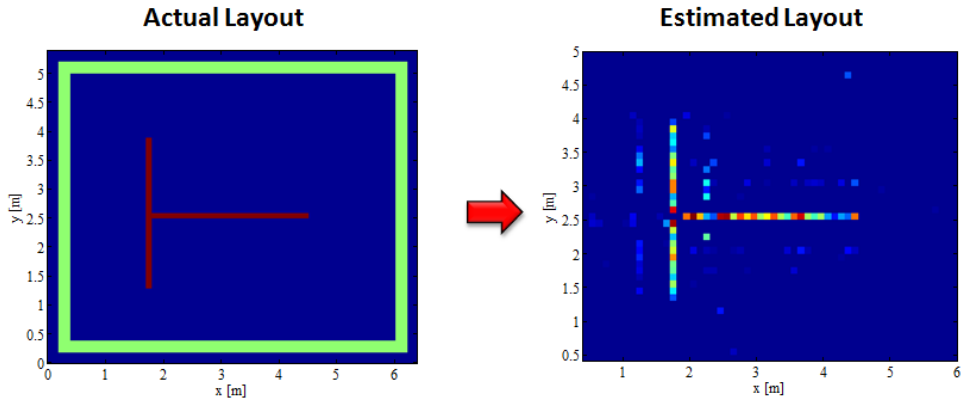

Figure 8: Layout reconstruction

2.5. Tracking Algorithm

The tracking algorithm is made of two parts. The first one provides the spatial map of targets' position, the second one uses this spatial map to estimate its movement inside the area of interest. The spatial map of the targets is obtained by using an efficient and accurate imaging algorithm based on a proper target model [41].

Such a model is considered for the formulation of the problem, referred to as Target-Based model (TB-model). The human body (the desired target) is modeled as a cylinder of proper dielectric property and is assumed to be infinitely long and invariant along y-axis. As well known, the problem of estimating the position of N targets, in terms of their coordinates from the scattered electromagnetic field is strongly nonlinear. However, it has been shown that, for this kind of applications, linear inversion schemes, neglecting the mutual interactions among the targets, work with success beyond the limits of the models they are based on [41]. Thanks to the linearity of the model, it is possible to adopt an algorithm characterized by low computational burden to achieve the number and position of the targets, which is auspicated for moving target applications. To this aim, a reconstruction procedure based on the Truncated Singular Value Decomposition (TSVD) inversion scheme is taken into account [9]. Moreover, the inversion algorithm exploits the previous estimated information (modeled scenario block) to correctly localize and track the persons and to remove the presence of spurious artifacts.

In order to filter out existing unknown static objects (as tables) and to focus out only on moving targets, a post-processing algorithms on reconstructed frames compatible with human motion (from 0.5 m/s to 5 m/s) is performed.

2.6. Life Signs Detection

Aim of this block is the detection of life signs, in particular the heartbeat and/or breathing. The idea is to illuminate by means of electromagnetic signals (in particular sinusoidal carrier at microwave frequencies) the zone of interest and to detect the presence of humans inside taking advantage from the modulation induced from the breastbone movement (a sufficiently periodic movement) on the reflected signal. So the added value of this block is the capability of detection of motionless people. An innovative signal processing procedure has been developed. The proposed procedure allows to process the available data, and to detect the presence of life signs, in real time. Such functionality makes the

proposed architecture a useful supporting tool in both civil and military applications. In fact it could be used to localize humans in trouble under ruins produced by landslides, earthquakes etc, or to localize motionless intruders in sensitive areas. More details about the life signs extraction are reported in Chapter 4.

Chapter 3

Moving Target Tracking

This Chapter describes the proposed measurement method for tracking of moving targets [42]. In particular, the section 3.1 briefly highlights the fundamental requirements of the measurement system configuration, while the later sections describe all operating steps of the measurement algorithm; for the sake of clarity, they are also sketched in the block diagram of Fig.9.

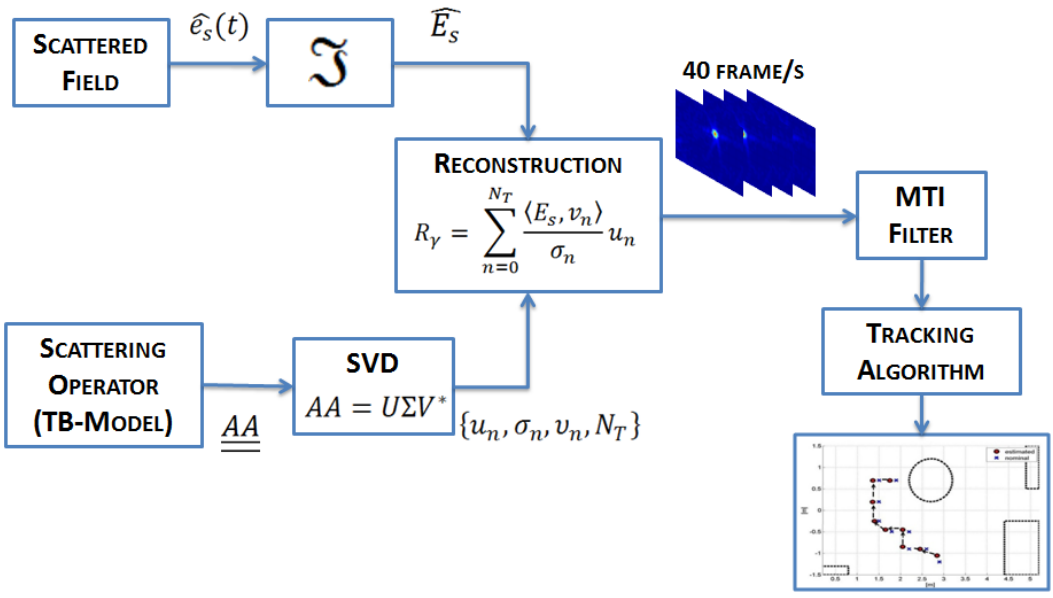

Figure 9: Block diagram of the proposed measurement method

Special emphasis is put both on the adopted scattering model and the linear inversion scheme, whose combined use makes it possible to correctly detect the presence of humans inside rooms or complex scenes.

3.1. Measurement System Configuration

The measurement system (MS) has to feature:

- a set of N_a identical transmitting and receiving antennas arranged on one or more lines with uniform spacing equal to $\lambda_{\min}/2$, where $\lambda_{\min}$ is the wavelength associated with the highest frequency involved in the measurement signal;
- a generation section that produces the electromagnetic signal to be transmitted;
- an acquisition section that digitizes the received electromagnetic signal.

MS can implement either a *multi-monostatic* or a *multistatic/multiview* approach. In the first case, each antenna acts both as a transmitter and receiver. In particular, an electromagnetic pulse with defined spectral characteristics is transmitted and received by a single antenna (monostatic approach); the same procedure is repeated for any other antenna of the set (multi-monostatic approach). As for the *multistatic/multiview* approach, a number of antennas act only as transmitters while the remaining ones act only as receiver. In particular, an electromagnetic pulse with defined spectral characteristics is transmitted by a single antenna and simultaneously received by a defined number of receiving antennas (multiview approach); the same procedure is repeated for any other transmitting antenna of the system (multistatic/multiview approach).

The considered measurement configuration is a multi-monostatic multifrequency. The acquisition system operates as a Stepped Frequency

Continuous Wave (SF-CW) sensor and collects the data as a function of frequency and position of each element of the antennas array.

3.2. Scattering model

The developed scattering model takes into account the scene shown in Fig.10. The measurement system, within which the sources of the incident field are located, is on the left, the wall is in the middle and the investigation domain, within which the movement of the targets has to be tracked, is on the right. The sources of the incident field $E_{inc}(\cdot)$ are being modeled as a filamentary current directed along y-axis, which is orthogonal to the plane of the investigation domain, they are located at the air/obstacle interface at $z = z_S$ and radiating within a frequency bandwidth $f \in [f_{\min}, f_{\max}]$.

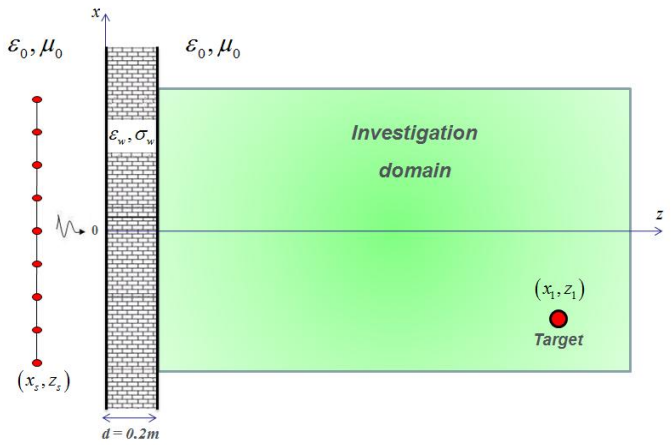

Figure 10: Geometric model of the considered problem.

The propagation medium includes three layers, the first and the last of which are considered as free-space, while the second layer represents the wall. In particular, a homogeneous and non magnetic wall characterized by dielectric permittivity ε_w and conductivity σ_w is considered, whereas d is its thickness. Of course, a more accurate wall model (involving several layers having

heterogeneous characteristics) could be used in order to allow a more rigorous reconstruction of the investigated scene in terms of resolution and position estimates; nevertheless, as confirmed by the results of actual experiments shown below, the adopted assumption does not prove too restrictive. The targets are located within an investigation domain $D = [-x_{\min}, x_{\min}] \times [z_{\min}, z_{\max}]$.

The desired target is approximated by means of a cylinder characterized by unchanging radius (according to the size of human body section); it is so possible to exploit the a priori information about the target, i.e. its geometrical features. In particular, for all tests described in the following chapters, the radius a of the cylinder has been set equal to $20cm$, according to the radius of the average human being.

Moreover, the targets have been considered of perfect electrical conductor (PEC), and assumed to be infinitely long and invariant along y-axis (note the target is the human inside the region of interest). This is a reasonable assumption because a human body contains a percentage of water, i.e. a strong scatterer, greater than 60%. As concern the hypothesis made on the vertical size, it can be noticed that human body dimensions are greater than the wavelength required by the above approximation (according to what stated in [41]). Both hypotheses allow the reduction of a very complex 3D through the wall imaging problem to a more simple 2D configuration.

3.3. Imaging Algorithm

TWI is a typical inverse scattering problem, the implemented procedure is based on a microwave tomographic approach [43]. Although inverse scattering problems are nonlinear [44], a linear reconstruction algorithm based on the Kirchhoff approximation is considered (as we plan to deal with strong scattering objects), it allows to meet all the main requirements for a TWI problem.

However, the choice of a linear inversion scheme allows to achieve stability against the noise, to avoid the local minima problem, and to ensure computational efficiency, which is required for operation within a large (in terms of wavelength) investigation domain. Most importantly, a deep analysis of the mathematical relationship to be inverted allows to foresee the performance that is achievable while reconstructing. Many linear inversion algorithms can be found in the literature, in particular, here, the Truncated Singular Value Decomposition (TSVD) of the linearized scattering operator is exploited for obtaining a regularized reconstruction of scenario [9].

The adopted scattering model (TB-model) is capable of taking fully into account the complex electromagnetic phenomena related to actual scenes with a reduced computational burden. The core novelty of the method is related to the construction of scattering operator, that takes into account the geometrical features of the unknown/searched targets (i.e. the human body), thus allowing better estimates of target position and a reduced number of unknowns if compared to other traditional scattering models [45], [46]. Differently from the approaches already presented in the literature, the model allows the evaluation of the current induced in the targets as those circulating on the surface of a cylinder modeling the target itself, thus assuring a lower computational burden. The induced current is, in fact, evaluated for the whole surface of the target; in the other approaches, instead, the evolution of the current is gained by means of a number of infinitely long wires covering the target surface.

As stated above, estimating the position of N_D targets, in terms of their coordinates (x_n and z_n, with $n = 1,...,N_D$), from the scattered electromagnetic field, is a strongly nonlinear problem. The nonlinearity mainly relies on the fact that the induced current in a single point of the domain depends on the induced current in each other point of the domain. It is worth noting that the number of target does not have to be *a priori* known, and its value can be determined in the

successive steps by means of the significant peaks singled out in the reconstructed image.

Due to the above hypotheses, the electric scattered field is still linearly polarized along the axis y and it can be written as

$$E_S\left(x_0, z_0\right) = -j\omega\mu \int_D G\left(x_0, z_0, x, z\right) J_{ind}\left(x, z\right) dx\, dz \tag{3.1}$$

where $\left(x_0, z_0\right)$ are the coordinates of the observation position (*i.e.*, the position of a receiving antenna), $G\left(x_0, z_0, x, z\right)$ is the Green's function associated with the modeled scenario of Fig.10, accounting also for the presence of the wall, and $J_{ind}\left(x, z\right)$ is the induced current on the modeled target (PEC), that contains the unknowns. With regard to the inducted current, it is worth noting that the TB-model operates in such a way as to define its values more accurately. The reconstruction of the target (in particular, its shape) is, typically, accomplished by means of the superposition of a defined number of infinitely long filaments of AC current flowing on its surface; on the contrary, in the adopted model, the target is reconstructed through cylinders. In other words, employed expression of $J_{ind}(x, z)$ is the induced current on the cylinder centered in $\left(x, z\right)$.

As shown in [45]–[47], linear inversion schemes prove suitable to face this kind of problem. Specifically, introducing the distributional function γ defined as

$$\gamma\left(x, z\right) = \sum_{n=1}^{N_D} \delta(x - x_n)\delta(z - z_n) \tag{3.2}$$

where N_D is number of targets, the scattered field can be rewritten as

$$E_S\left(x_0, z_0\right) = -j\omega\mu \int_D G\left(x_0, z_0, x, z\right) J_{ind}\left(x, z\right) \gamma\left(x, z\right) dxdz \tag{3.3}$$

The function γ, thus, can be used to locate the target position (in particular the center of the cylinder) within the investigation domain. Equation (3.3) becomes a superposition integral that relates the scattered field to the actual unknown distributional function γ through a linear integral relationship. It is so possible to significantly limit the computational burden for the desired estimation purposes; a desirable condition for moving target applications.

The desired values of γ can be obtained as the solution of the linear system:

$$E_S = \mathbf{AA}(\gamma) \Rightarrow \gamma = \mathbf{AA^{-1}}\left(E_S\right) \tag{3.4}$$

where $\mathbf{AA}$ is the integral operator numerically evaluated by means of a Finite Difference Time Domain (FDTD) based code, while E_S stands for the measured scattered field.

Being ill-posed [9], the considered problem needs a regularization procedure. In particular, an inversion scheme based on TSVD has been adopted to obtain the inverse operator $\mathbf{AA^{-1}}$, by means of which the desired image (i.e., a single snapshot of the current distribution in the investigated two-dimensional domain) can be gained. More specifically, the integral operator is factorized as

$$\mathbf{AA = U\Sigma V^*} \tag{3.5}$$

where $\mathbf{U}$ is a square unitary matrix, $\mathbf{\Sigma}$ is a diagonal matrix with nonnegative real numbers on the diagonal entries, and $\mathbf{V^*}$ stands for a square unitary matrix, that is the conjugate transpose of $\mathbf{V}$. From eq. (3.5) it is easy to evaluate the expression of $\mathbf{AA^{-1}}$:

$$\mathbf{AA}^{-1} = \mathbf{V}\Sigma^{-1}\mathbf{U}^* \tag{3.6}$$

It is worth noting that the factorized integral operator $\mathbf{AA}$, as well as its inverse $\mathbf{AA^{-1}}$, depends only on

- modeled investigation domain (as accounted for by the Green's function)
- the inducted currents (due to the discretization of the investigation domain and the model assumed for the targets and numerically evaluated)
- the sources of the incident field.

It can thus be evaluated off-line by means of numerical algorithms, thus allowing a further reduction of the computational burden and making real-time measurements much more feasible. In particular, to take into account the finiteness of the wall dimensions, which can cause the arising of spurious artifacts due to the edge diffraction, the Green's function has been numerically evaluated, exploiting the information on the electromagnetic parameters of the wall and the internal layout provided by the functional blocks described in §2.3 and §2.4.

In this way, the Green's function takes into account modeled scenario, the inducted currents, due to the discretization of the investigation domain and the model assumed for the targets, can be numerically evaluated and scattering operator built.

A graphical representation of construction method of scattering operator in TB-model is shown in the Fig.11.

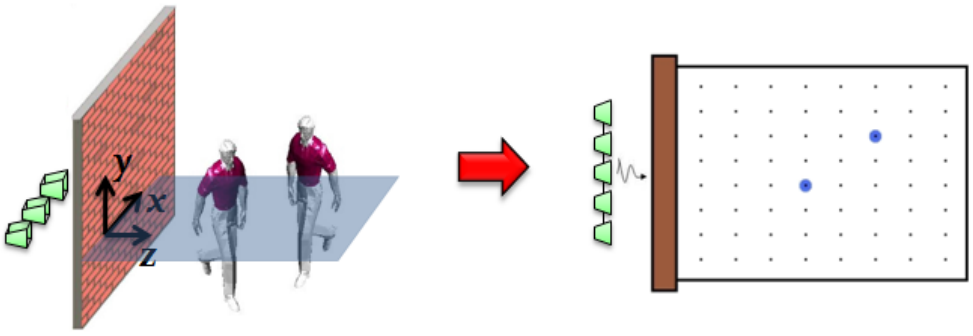

Figure 11: TB-model Operator Construction

A regularized solution R_γ of the equation (3.4) can be written as

$$R_\gamma = \sum_{n=0}^{N_T} \frac{\langle E_S, v_n \rangle}{\sigma_n} u_n \tag{3.7}$$

where N_T is the truncation index. Moreover, the set $\{\sigma_n\}_{n=0}^{\infty}$ denotes all singular values, ordered in a non increasing sequence, whereas $\{u_n\}_{n=0}^{\infty}$ and $\{v_n\}_{n=0}^{\infty}$ form orthonormal bases in the unknowns and data spaces, respectively [9]. Particular attention has to be paid to the selection of the value N_T; it depends both on the behavior of the singular values and the tolerable noise level on data. The presence of noise, in fact, prevents the use of all singular values needed for an accurate snapshot; the bigger N_T, the finer resolution, the higher the effect of noise on the final result. With respect to the proposed method, N_T has suitably been chosen according to the available SNR. As a result, the higher values of R_γ are associated with the locations of the investigation domain actually occupied by human targets; on the contrary, the absence of target gives rise to low levels of dimensionless distributional function γ.

Better performance of the method can be achieved if the MS, implementing a multi-monostatic approach, operates as a stepped frequency continuous wave sensor. In particular, the acquisition system collects the data as a function of frequency and position of each element of the antennas array. The step Δf of frequency sweep has been set according to the Shannon sampling theorem, since it depends on the extent Δz, i.e. along the z-axis, of the investigation domain [48]:

$$\Delta f \leq \frac{B}{N_{freq}} \qquad \text{where} \qquad N_{freq} = \frac{(k_{\min} - k_{\max})}{\pi} \Delta z \tag{3.8}$$

where B stands for adopted frequency bandwidth, while $k_{\min}$ and $k_{\max}$ are equal respectively to $2\pi/\lambda_{\min}$ and $2\pi/\lambda_{\max}$. In particular, for each antenna of the array and frequency value in the bandwidth B, the acquisition system transmits and

receives an electromagnetic signal. The procedure waits for the construction of the integral operator $\mathbf{AA}$, a $N \times M$ matrix where $N = N_{freq} \times N_{obs}$, with N_{freq} number of frequencies and N_{obs} number of observation points, while $M = n_x \times n_z$ stands for the number of cells used to discretize the investigation domain in both directions. Each element of the operator represents the field scattered by a cylinder located at (x_n, z_n) in the investigation domain when it is exposed to an incident field of frequency f^*, generated by an antenna placed in (x_s, z_s), as shown in Fig.10. In other words, each element of $\mathbf{AA}$ is a solution of (3.4) with γ a priori established, i.e. N stands for the number of equations needed to determine the field scattered by a cylinder in a defined point of the investigation domain. This approach has been adopted both in the construction of the integral operator $\mathbf{AA}$ and data acquisition. Finally the inverse operator $\mathbf{AA}^{-1}$ obtained with TSVD has been processed with measured data according to (3.7). According to what stated in [9], the adopted frequency diversity is required to achieve the desired resolution in image reconstruction and obtain a better SNR.

These considerations explain the dependence of the frequency sampling step from the size of the investigation domain. So, if the minimum number of frequencies is set by the Shannon's theorem, it can be observed that a very large number of frequencies does not provide advantages in image reconstruction, since the associated equations would be dependent from one another and provide no useful information.

3.4. Detection and Target Tracking

As stated above, each obtained snapshot provides a reconstructed spatial map of the investigation domain as well as the position of the target, which is a key step for tracking purposes. Since the investigation domain has been modeled in the hypothesis of free space, the presence of furniture or other fixed objects in the

scene gives rise to artifacts that could prevent the correct localization of the targets. As an example, let us consider the scene shown in Fig.12; it consists of a table and a cupboard within the investigation domain.

The presence of the table makes the location of the target behind it more difficult from the analysis of a single snapshot (Fig.13a-c); in particular, the artifacts due to its presence should completely hide the target.

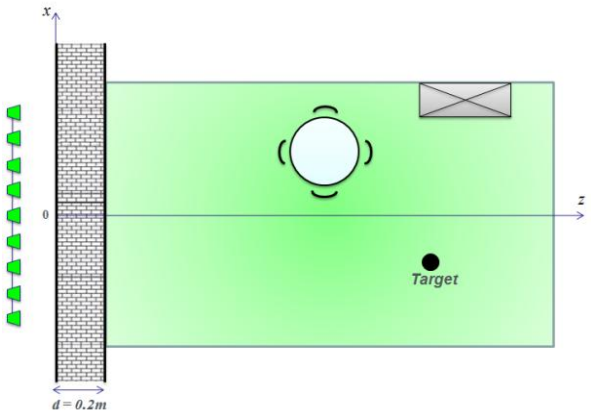

Figure 12: Geometric model in the presence of furniture.

To overcome this limitation, the detection and tracking of the target is accomplished through a Moving Target Indicator (MTI) filter (Fig.14a and Fig.14b) that removes all static targets (tables, cupboards and walls).

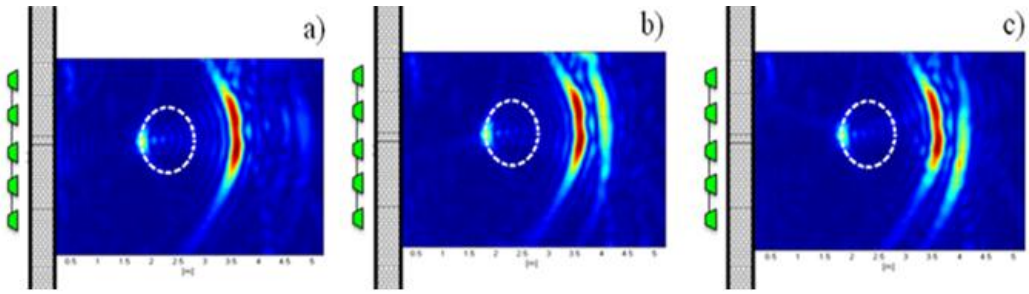

Figure 13: Consecutive snapshots obtained in the presence of furniture; the effect due to the presence of the table makes target location difficult to be achieved

Clearly, the MTI filter is not able to remove the mutual interactions between moving target and static target, but this effect is strongly mitigated by adopted

imaging algorithm, which takes into account the internal layout evaluating numerically the Green's function.

This way, artifacts related to stationary items are removed from the reconstructed scene. All that is stationary during the measurement process does not appear in the reconstructed scene, while effects due to the moving targets are preserved.

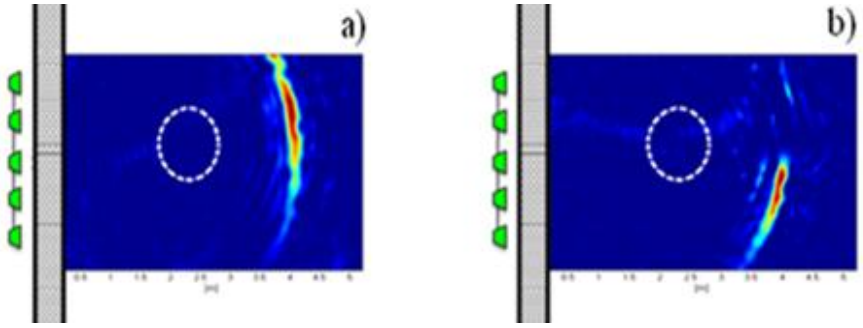

Figure 14: Application of the MTI Filter to the snapshots of Fig.10;

To further improve the measurement algorithm, a suitable threshold (Fig.15) is applied to each snapshot to remove the remaining artifacts due to the actual investigation domain, noise and regularization [45].

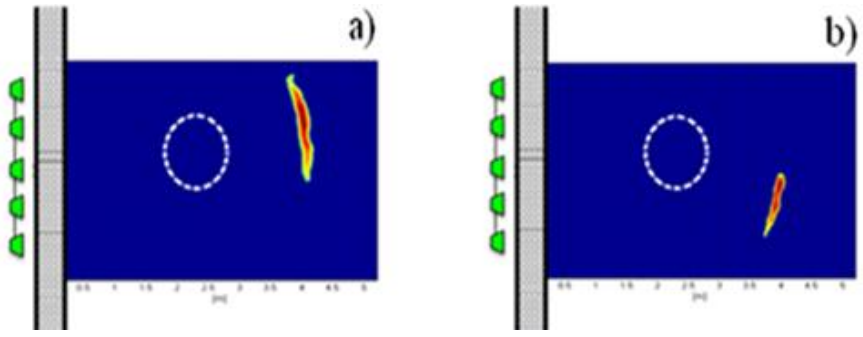

Figure 15: Snapshots of Fig.11 after the application of the threshold procedure.

The procedure automatically localizes, for each snapshot, the moving targets' position extracting the relative maximum points in the reconstructed image.

Moreover, the tracking algorithm, storing the previous states, automatically provides the instantaneous direction and velocity of each target.

Finally, thanks to the availability of the position of the targets in each snapshot, their direction and velocity is automatically evaluated (automatic tracking procedure).

To achieve reliable results, the moving targets have to be stationary in the acquisition interval, i.e. the time taken by the measurement station to digitize the scattered electromagnetic field. It is worth noting that the method works with success only if the trajectories of moving targets do not present intersections with one another (i.e. the minimum distance between two different trajectories is lower than an human step); this way, the trajectory of each target can be defined as the curve connecting all the successive positions the distance of which results lower than one human step.

3.5. TB Model: comparative analysis

To assess the performance of the TB model, its performance has been compared with those gained by means classical technique [45], [46]. In particular in [45] the problem of imaging “thin” (much smaller than the wavelengths of the exploited incident radiation) metallic cylinders from the knowledge of the scattered far field has been faced by means of a linear δ-function approach. The results of the comparison are given in Fig.16, in particular in Fig.16a is show the comparison in the case of a target in the presence of a single wall between the multisensor system and the target. The obtained performances are excellent in both cases. It is worth noting that the imaging technique based on thin cylinders approximation reconstructs the edge of the target causing a small localization error equal to the radius of the considered cylinder to approximate the target. This error is clearly negligible. In Fig.16b and Fig.16c the presence of four walls is considered, in the first case a single target is present in the scene, in the second case two targets are considered. The obtained results highlight the superior performance of TB-model in terms of mutual interactions and multipath, which

give rise to spurious artifacts and false alarms, in particular the TB model takes into account the interactions between moving target and the external walls, so no artifacts appear in the investigation domain.

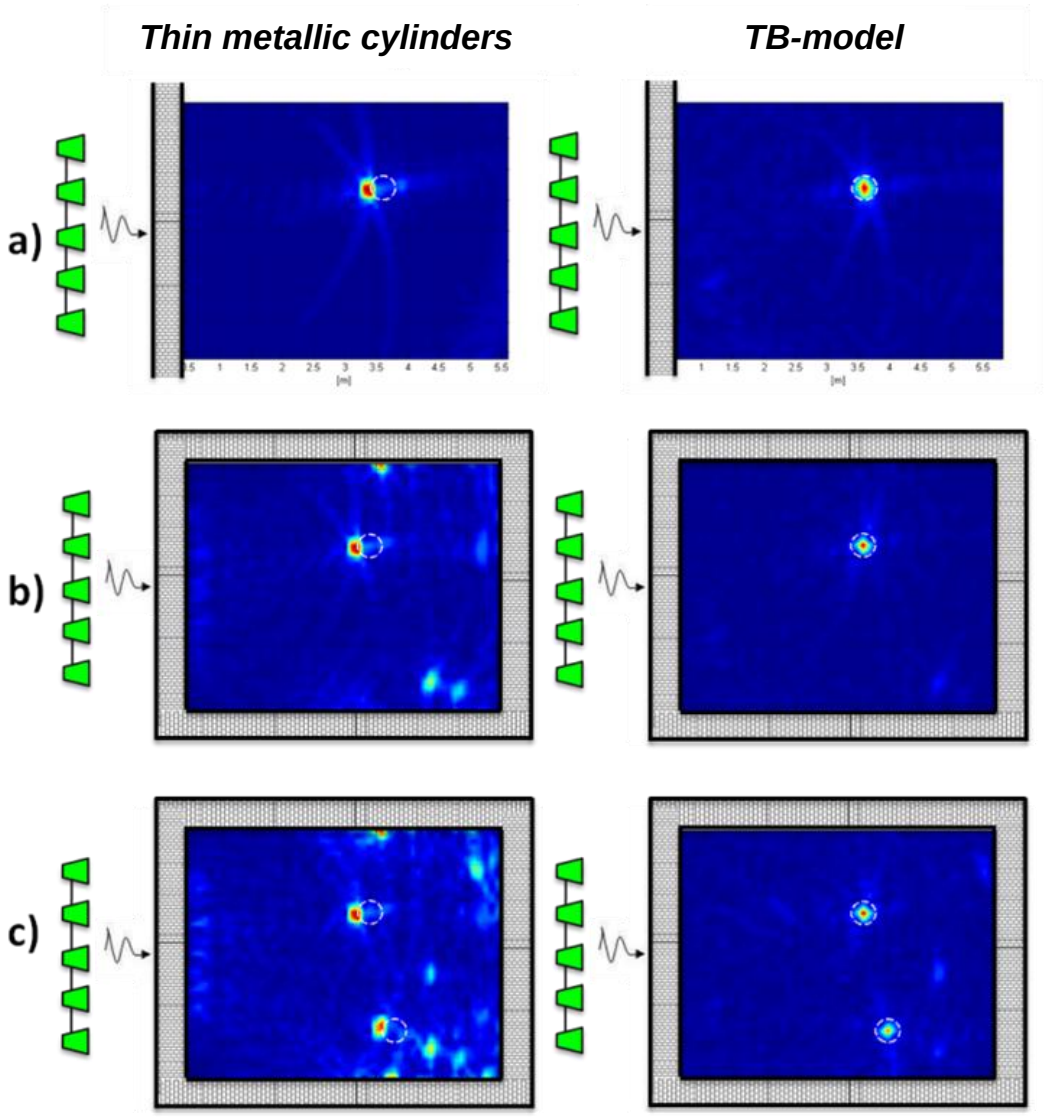

Figure 16: Comparison of obtained results; a) Single target and single wall; b) Single target and four walls; c) Two targets and four walls.

Chapter 4

Life Signs Detection

In this Chapter, as mentioned before, a new measurement method for through-the-wall detection of life signs is derived [49]-[50]. The method analyzes the phase modulation that a sinusoidal signal, generated by means of a proper continuous wave microwave transceiver, undergoes when reflected by the chest periodic displacement associated with breathing, as shown in the reference scenario of Fig.17. It takes advantage of a suitable spatial smoothing decorrelation strategy applied to the traditional algorithm for multiple signal classification (MUSIC), mandated to single out the spectral components of the received phase signal. The attention is specifically focused on the spectral content characterizing the backscattered electromagnetic signal due to its reflection from a moving chest. The model is described with references to a generic continuous-wave (CW) system, which involves two different antennas for signal transmission and reception, respectively.

In particular, in the first section the rationale of the overall echo model is presented and the adopted transmitted waveform modeling is derived; in the second section theoretical details concerning the MUSIC algorithm are given. The last section describes all operating steps of the proposed measurement algorithm.

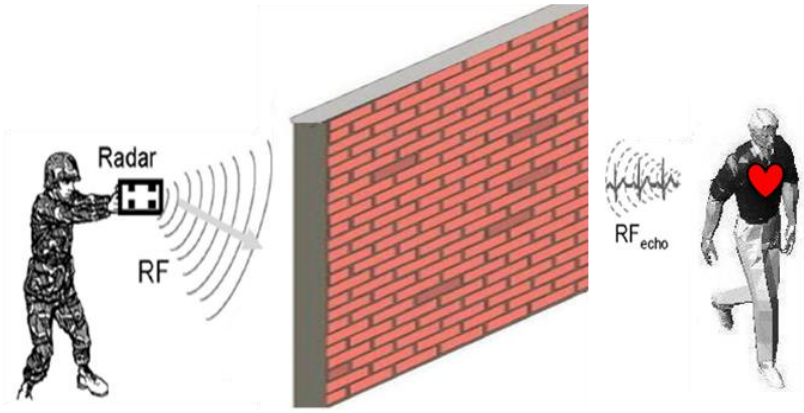

Figure 17: Reference Scenario

4.1. Backscattered signal model

In the assumption that amplitude variations can be neglected, the evolution versus time of a signal T generated by a generic CW system can be expressed as:

$$T(t) = \cos\left(2\pi ft + \phi(t)\right) \tag{4.1}$$

where f is the signal frequency and $\phi(t)$ stands for the phase noise component of the local oscillator.

Let us suppose that the signal T is backscattered by a target placed at a distance equal to d_0 from the CW system, and characterized by a local time-varying displacement, referred to as $x(t)$, related to the chest movement. In this condition, the total distance between the transmitting and receiving antenna of the CW system is equal to

$$2d(t) = 2d_0 + 2x(t) \tag{4.2}$$

The chest movement $x(t)$ can be expressed as the sum of two different contributions, $x_r(t)$ and $x_h(t)$, which represent body movements associated with respiration and heartbeat; for sake of the clarity, the contributions can be

expressed as $x_r(t) = m_r \sin(\omega_r t)$ and $x_h(t) = m_h \sin(\omega_h t)$, i.e. sinusoidal signals with amplitudes m_r and m_h and angular frequencies ω_r and ω_r respectively [31].

According to what stated in [31], the received signal R can be approximated as:

$$R(t) \cong \cos\left(2\pi ft - \frac{4\pi d_0}{\lambda} - \frac{4\pi x(t)}{\lambda} + \phi\left(t - \frac{2d_0}{c}\right)\right) \tag{4.3}$$

where c stands for the light propagation velocity (free space propagation is supposed) and λ is the signal wavelength, equals to c/f. In particular, the received signal shows a time evolution similar to that of $T(t)$, but a time delay due to two different contributions: the former is related to the nominal distance d_0 the latter is associated with the periodic motion of the target.

According to the simplified block diagram of a Doppler-radar system shown in Fig.18, if the received signal is multiplied by a local oscillator signal, derived from the transmitted signal, proper information about the target periodic motion can be gained [29]. This approach keeps the phase noise of the two considered signals highly correlated, while the receiver pre-selector provides for a tunable filter to reject out-of-band interference that would create unwanted responses.

As shown in Fig.18, two branches can be distinguished, the in phase (I) branch and the in quadrature (Q) branch. With regard to the I branch, the signal is multiplied by a sinusoidal carrier, the frequency of which is equal to that of the transmitted signal. The multiplication gives rise to both a baseband component and a high-frequency component. A low-pass filtering is carried out to retain only the baseband component (also called the I component). As for the Q branch, the orthogonal version (also called the Q component) of the aforementioned

baseband component is furnished as a result of similar operations. In particular, the I and Q components can be written as

$$B_I(t) = \cos\left[\theta + \frac{4\pi x(t)}{\lambda} + \Delta\phi(t)\right] \tag{4.4}$$

$$B_Q(t) = \cos\left[\theta - \frac{\pi}{2} + \frac{4\pi x(t)}{\lambda} + \Delta\phi(t)\right] \tag{4.5}$$

where

$$\theta = \frac{4\pi d_0}{\lambda} + \theta_0 \qquad \text{and} \qquad \Delta\phi(t) = \phi(t) - \phi\left(t - \frac{2d_0}{c}\right) \tag{4.6}$$

stand for the constant phase shift due to the distance d_0 and the residual phase noise.

The evolution $\gamma(t)$ of the phase of the received signal can straightforwardly be gained by applying the expression

$$\gamma(t) = a\tan\left(\frac{B_Q(t)}{B_I(t)}\right) = \theta + \frac{4\pi x(t)}{\lambda} + \Delta\phi(t) \tag{4.7}$$

to the obtained baseband components, where $a\tan(\cdot)$ stands for the arctangent operator [51].

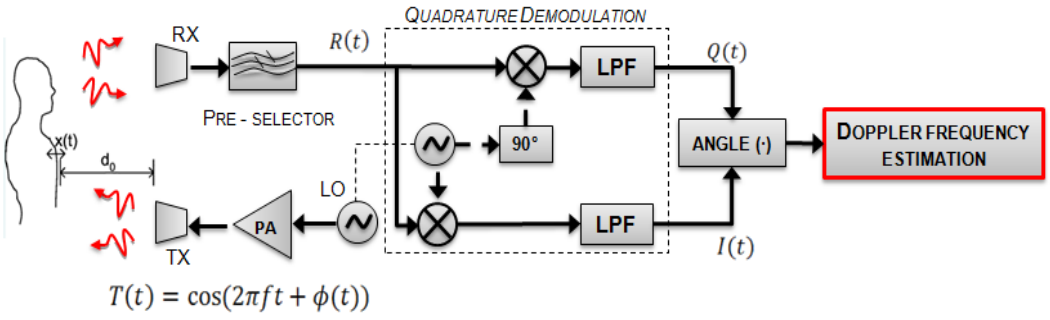

Figure 18: Simplified Doppler radar system block diagram.

4.1.1. Spectral Analysis

From the theory of Fourier Series any time-varying periodic displacement $x(t)$ can be viewed as the combination of a series of single-tone signals, [30]-[31]. Therefore, without loss of generality $x(t)$, is assumed in the following to be a single tone signal, i.e. $x(t) = m\sin(\omega t)$. Of course, ω denotes here the frequency of the chest movement.

The phase-modulated signal can be now represented as

$$\begin{aligned} B(t) &= \Re e\left\{B_I(t) + jB_Q(t)\right\} = \Re e\left\{e^{j\left(\frac{4\pi m\sin(\omega t)}{\lambda}\right)} e^{j[\theta+\Delta\phi(t)]}\right\} = \\ &= \cos\left[\theta + \frac{4\pi m\sin(\omega t)}{\lambda} + \Delta\phi(t)\right] \end{aligned} \tag{4.8}$$

Then, if the exponential term is expanded using Fourier series

$$e^{j\left(\frac{4\pi m\sin(\omega t)}{\lambda}\right)} = \sum_{n=-\infty}^{\infty} J_n\left(\frac{4\pi m}{\lambda}\right) e^{jn\omega t} \tag{4.9}$$

where $J_n(x)$ is the n[th]-order Bessel function of the first kind, an interesting Fourier-series based representation of the phase-modulated signal in (4.8) can be

$$B(t) = \Re e\left\{\sum_{n=-\infty}^{\infty} J_n\left(\frac{4\pi m}{\lambda}\right) e^{jn\omega t} e^{j[\theta+\Delta\phi(t)]}\right\} = \sum_{n=-\infty}^{\infty} J_n\left(\frac{4\pi m}{\lambda}\right)\cos(n\omega t + \phi) \tag{4.10}$$

where $\phi = \theta + \Delta\phi(t)$ is the total residual phase.

Based on (4.10), the phase-modulated baseband signal is decomposed into frequency components with n times the basic frequency of the periodic movement.

Accordingly, the spectral content of the signal (4.10) can be simply analyzed in the frequency domain, giving in a very simple way important indications on the nature of the detected movements. As it can be seen from Fig.19, in the frequency domain, the received signals exhibits delta-like behaviors in all those frequencies which are n times the basic frequency of the chest movement $x(t)$, thus allowing to detect the human presence by observing the spectral content of the measured signal.

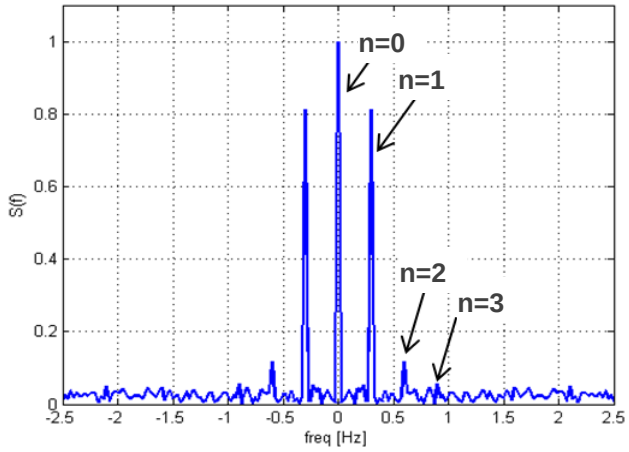

Figure 19: Spectrum of the baseband signal of (4.10)

4.2. MUSIC Algorithm

Based on the orthogonal subspace projection proposed in [52], MUSIC algorithm can be classified as a noise subspace frequency estimator. In particular, it estimates the autocorrelation matrix using an eigenspace method, and works in the assumption that the signal of interest, $x(n)$, consists of the sum of r complex exponentials in the presence of white Gaussian noise. Given an autocorrelation matrix with dimensions equal to $M \times M$ (M being the number of digitized samples), if the eigenvalues are sorted in a decreasing order, the r eigenvectors corresponding to the r largest eigenvalues point out the signal subspace. Let us

consider a random sequence given by r independent complex sine waves buried in noise:

$$x(n) = \sum_{i=1}^{r} s_i(n) + w(n) = \sum_{i=1}^{r} A_i e^{j(\omega_i n + \varphi_i)} + w(n) \tag{4.11}$$

where $w(n)$ is the additive white noise. The acquired sequence consists of M samples:

$$\mathbf{x}(n) = \begin{bmatrix} x(n) \\ . \\ . \\ . \\ x(n+M-1) \end{bmatrix} = \mathbf{A}(\omega)\mathbf{S}(n) + \mathbf{W}(n) = \tag{4.12}$$

$$\begin{bmatrix} 1 & 1 & ... & 1 \\ e^{j\omega_1} & e^{j\omega_2} & ... & e^{j\omega_r} \\ . & . & ... & . \\ . & . & ... & . \\ e^{j(M-1)\omega_1} & e^{j(M-1)\omega_2} & ... & e^{j(M-1)\omega_r} \end{bmatrix} \times \begin{bmatrix} A_1 e^{j(\omega_1 n + \varphi_1)} \\ A_2 e^{j(\omega_2 n + \varphi_2)} \\ . \\ . \\ A_r e^{j(\omega_r n + \varphi_r)} \end{bmatrix} + \begin{bmatrix} w(n) \\ w(n+1) \\ . \\ . \\ w(n+M-1) \end{bmatrix}$$

If each column $\begin{bmatrix} 1 & e^{j\omega_i} & ... & ... & e^{j(M-1)\omega_i} \end{bmatrix}^T$ is referred to as $\mathbf{a}(\omega_i)$, the matrix $\mathbf{A}(\omega)$ can be written as $\begin{bmatrix} \mathbf{a}(\omega_1) & \mathbf{a}(\omega_2) & ... & ... & \mathbf{a}(\omega_r) \end{bmatrix}$. The autocorrelation matrix of the measured data vector $\mathbf{x}(n)$ can, thus, be expressed as the sum of the autocorrelation matrices of the signal $s(n)$ and the noise $w(n)$ as:

$$\mathbf{R} \triangleq \mathrm{E}\left\{\mathbf{x}(n)\mathbf{x}^*(n)\right\} = \mathbf{R_S} + \mathbf{R_W} = \mathbf{APA^H} + \sigma_w^2 \mathbf{I} \tag{4.13}$$

where H denotes the conjugate transpose operator, the diagonal matrix $\mathbf{P}$ stands for the correlation matrix of the input sinusoidal signals and σ_w^2 is the noise power.

According to what stated in [53], the autocorrelation matrix $\mathbf{R}$ can be decomposed as

$$\mathbf{R} = \mathbf{U_S}\mathbf{\Lambda_S}\mathbf{U_S^H} + \mathbf{U_W}\mathbf{\Lambda_W}\mathbf{U_W^H} \tag{4.14}$$

where $\mathbf{\Lambda_S} = diag\left(\lambda_i + \sigma_w^2\right)$ (i.e. a diagonal matrix whose entries are the r largest eigenvalues with $\lambda_1 \geq \lambda_2 \geq ... \geq \lambda_r$), $\mathbf{U_S} = \left[\mathbf{u_1} \quad \mathbf{u_2} \quad \mathbf{...} \quad \mathbf{...} \quad \mathbf{u_r}\right]$ is the signal subspace and contains the r eigenvectors corresponding to the r largest eigenvalues, $\mathbf{\Lambda_W} = diag\left(\sigma_w^2\right)$ and $\mathbf{U_W} = \left[\mathbf{u_{r+1}} \quad \mathbf{u_{r+2}} \quad \mathbf{...} \quad \mathbf{...} \quad \mathbf{u_M}\right]$ is the noise subspace.

In other words, the correlation matrix of the noisy signal can be written in terms of its eigenvalues and associated eigenvectors as:

$$\mathbf{R} = \sum_{i=1}^{M} \lambda_i^x \mathbf{u_i}\mathbf{u_i^H} = \sum_{i=1}^{r}\left(\lambda_i + \sigma_w^2\right)\mathbf{u_i}\mathbf{u_i^H} + \sum_{i=r+1}^{M} \sigma_w^2 \mathbf{u_i}\mathbf{u_i^H} \tag{4.15}$$

From Equation (4.15), the eigenvectors and the eigenvalues of the correlation matrix of the noisy signal can be partitioned into two disjoint subsets. The subset of eigenvectors $\{\mathbf{u_1}, \mathbf{u_2}, \ldots, \mathbf{u_r}\}$, called the principal eigenvectors, defines the signal subspace; signal vectors can be expressed as linear combinations of these principal eigenvectors. The second subset of eigenvectors $\{\mathbf{u_{r+1}}, \mathbf{u_{r+2}}, \ldots, \mathbf{u_M}\}$, whose eigenvalues are ideally equal to σ_w^2, defines the noise subspace. Since the signal and noise eigenvectors are orthogonal, it follows that the same considerations hold for signal subspace and noise subspace. As a consequence, also the sinusoidal signal vectors, which are in the signal subspace, are orthogonal to the noise subspace, and it can be written that

$$\left\langle \mathbf{a}^{\mathbf{H}}(f_i)\mathbf{u}_{\mathbf{k}} \right\rangle = \sum_{l=0}^{M-1} u_k(l) e^{-j2\pi f_i l} = 0 \tag{4.16}$$

with $i = 1,...r$ and $k = r+1,...,M$.

Equation (4.16) implies that the desired frequency values of the r sinusoidal signals can be obtained by finding the zeros of the following polynomial function:

$$\sum_{k=r+1}^{M} \mathbf{a}^{\mathbf{H}}(f)\mathbf{u}_{\mathbf{k}} = 0 \tag{4.17}$$

In the MUSIC algorithm, the power spectrum estimate is defined as

$$P(f) = \sum_{k=r+1}^{M} \left| \mathbf{a}^{\mathbf{H}}(f)\mathbf{u}_{\mathbf{k}} \right|^2 \tag{4.18}$$

Since the zeros of $P(f)$ are ideally positioned at the frequency values of the sinusoids, it follows that the reciprocal of $P(f)$ has its poles at the same frequencies.

MUSIC spectrum, usually referred to as pseudo-spectrum, is defined as

$$P^{MUSIC}(f) = \frac{1}{\mathbf{a}^{\mathbf{H}}(f)\mathbf{U}_{\mathbf{W}}\mathbf{U}_{\mathbf{W}}^{\mathbf{H}}\mathbf{a}(f)} \tag{4.19}$$

In nominal conditions, its local maxima occur in correspondence to the frequency values of the sinusoidal components involved in the received signal, thus suitable estimates (also called MUSIC estimates) of the quantities of interest can be achieved.

As shown in [54], given the duration of the observation interval, the resolution and estimation accuracy of the MUSIC algorithm get worse upon the SNR's decreasing, while in a definite condition of noise, they improve for wider observation intervals. The associated computational burden is mainly due to the eigenvalues decomposition and location of the pseudo-spectrum local maxima.

4.3. Measurement Algorithm

In this section all operating steps of the proposed method for life signs detection, in the following referred to as *Advanced Music*, are described. In particular it enlists:

- data acquisition
- phase signal filtering
- spatial smoothing procedure
- signal subspace selection
- MUSIC algorithm

For the sake of clarity, they are also sketched in the block diagram of Fig.20.

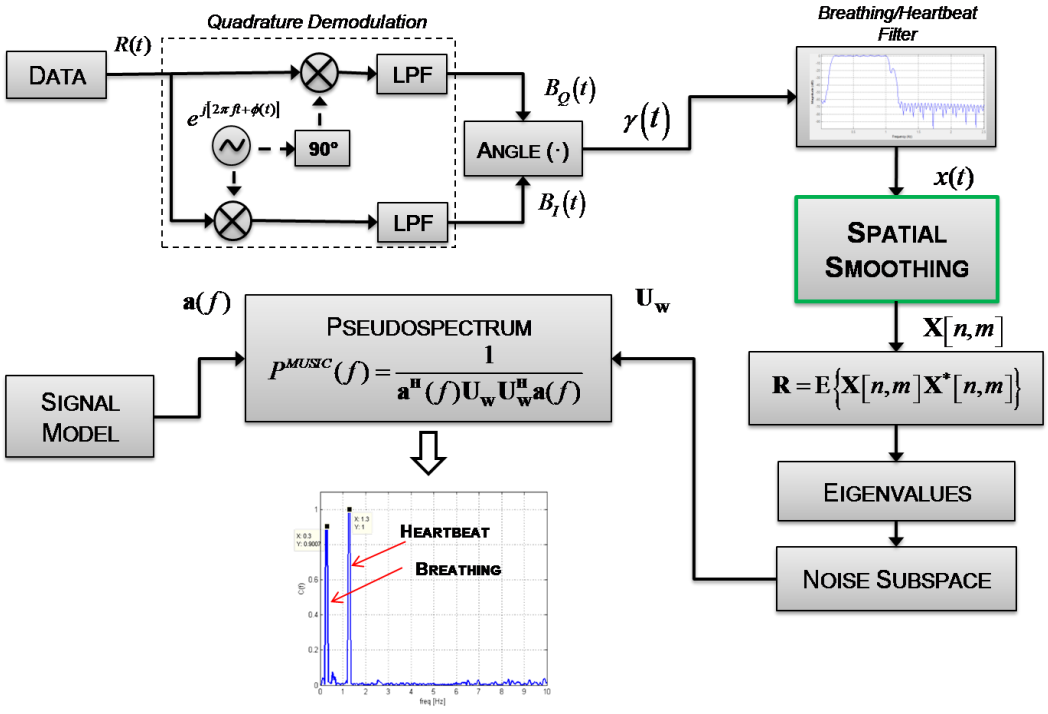

Figure 20: Block diagram of the proposed method for life signs detection

4.3.1. Data acquisition

The electromagnetic signal backscattered by the desired target is at first digitized by means of a suitable data acquisition system, the characteristics of which, in terms of sample rate and memory depth, have to be chosen appropriately. In particular, the use of a transceiver capable of assuring coherent phase relationship between transmitted and received signals should be advisable.

The main aim of the method is to detect low frequency phase modulation in the received signal, which is potentially associated with human beings. This way, a traditional demodulation scheme is at first applied to the backscattered signal, received by means of a suitable antenna.

The obtained signal $\gamma(t)$, as reported in (4.7), includes

- a DC signal due to the wall reflections;
- two separated Doppler components associated respectively with the breathing and heartbeat;
- noise.

4.3.2. Phase signal filtering

For a successful and straightforward application of the MUSIC algorithm, the phase signal is passed through a suitable band-pass filter, tuned on the frequency band peculiar to breathing and heartbeat and capable of rejecting the DC component. The use of a band-pass filter having narrow bandwidth and high stop-band attenuation is recommended. In particular, as typical medical data confirm that no life signs directly related to breathing and heartbeat are present outside the band $[0.1 \div 3] Hz$, a digital finite impulse response (FIR) filter with the same bandwidth and stop-band attenuation greater than 60 dB is adopted. Since only phase information is of interest, the filtered signal is normalized in order to limit some undesired amplitude modulation.

In [50] the MUSIC algorithm has been adopted to gain the spectral content of the phase of the received signal, thus detecting possible vital signs. In particular, the filtered phase signal has acted as the input sequence $x[n]$ for the MUSIC algorithm.

4.3.3. Spatial smoothing procedure

To make the proposed method outperform the old version, described in [50], a spatial smoothing procedure (in the following referred respectively to as temporal and sample decorrelation) has been implemented and applied to the filtered phase signal in order to increase the signal-to-noise ratio, Fig.21. To this aim, the adopted procedure allows improving the robustness of the considered signal model since it takes into account the non-perfect periodicity of the received signal.

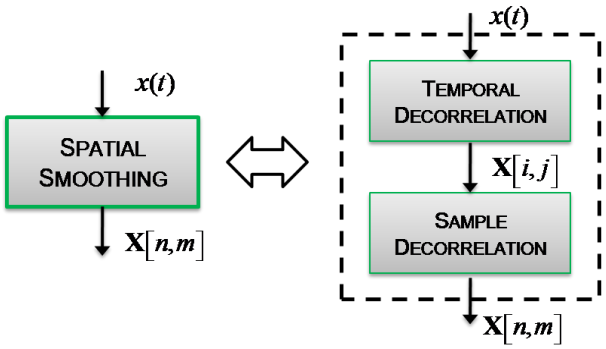

Figure 21: Spatial smoothing procedure

This result is obtained by a smart procedure of smoothing and an appropriate choice of the rank of the signal subspace. Fig.22 shows a graphical representation of the adopted decorrelation techniques.

The temporal decorrelation consists in dividing the whole array of M filtered phase samples in several blocks; the number N_{blocks} of the obtained blocks can thus be written as

$$N_{blocks} = \frac{T}{T_{block}} \tag{4.20}$$

where T stands for the whole observation interval and T_{blocks} is the time duration of each block. In order to set the value of T_{blocks}, the lowest typical value ($0.3Hz$) of breathing frequencies is taken into account. As a consequence, each burst lasts enough to contain at least one period of the breathing signal, i.e.

$$T_{block} \cong T_{breath} \tag{4.21}$$

where $T_{breath} \cong 3s$.

The sample decorrelation exploits the oversampling factor usually involved in the digitization of the received signal. In particular, an under-sampling factor α that satisfies the relation

$$f_x = \frac{f_{sample}}{\alpha} \geq 2B \tag{4.22}$$

is determined; $f_{sample} = \frac{M}{T}$ is the sampling rate of the received signal, B is the unilateral band of the breathing signal, while f_x is the new sampling rate. As a consequence, each block determined during the temporal decorrelation stage is divided into α new arrays, each of which corresponds to an α-decimated version of the original block; moreover, the index of each decimated array defines the index of first sample of the block adopted its generation (Fig.22).

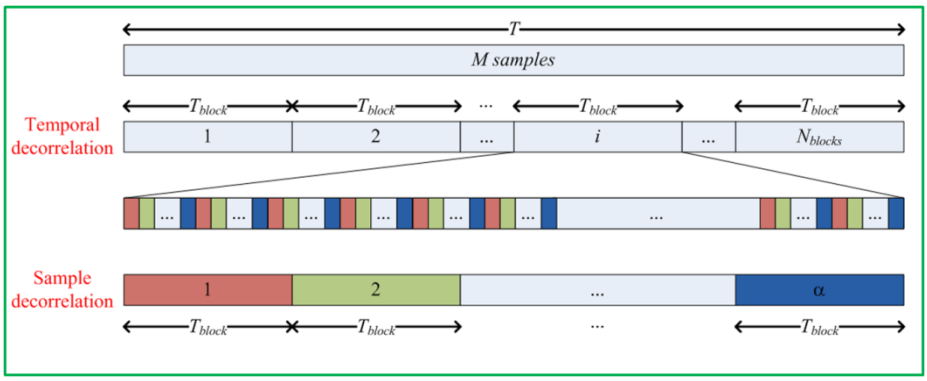

Figure 22: Adopted decorrelation technique.

The $N_{blocks} \cdot \alpha$ sequences of samples obtained after the sample decorrelation can be collected as the rows of a matrix $\mathbf{X}$, the columns of which contain the samples of the decimated filtered phase. The experimental (actual) autocorrelation matrix of the phase signal can thus be gained from the matrix $\mathbf{X}$ according to

$$\mathbf{R} = \mathrm{E}\left\{\mathbf{X}[n,m]\mathbf{X}^{*}[n,m]\right\} \tag{4.23}$$

where $n = 0,1,...,(N_{blocks} \cdot \alpha - 1)$ and $m = 0,1,...N_{spb}$, N_{spb} being the number of phase samples included in each α-decimated array.

Thanks to the adopted smoothing procedure, a significant increase in terms of number of eigenvalues is achieved. $N_{blocks} \cdot \alpha$ eigenvalues corresponding to the signal space can, in fact, be determined, thus successfully improving the signal-to-noise ratio. As an example, Fig.23 shows the improvement in terms of number of eigenvalues; in particular 4 blocks have been considered, each of which decimated by 5.

Moreover, the adopted strategy can assure a significant reduction of the computational burden, thus making the proposed method more attractive for real-time applications. Specifically, the autocorrelation matrix evaluated in (4.23) has $M \times M$ dimensions; after the decorrelation stages the autocorrelation matrix $\mathbf{R}$ has dimensions $N_{spb} \times N_{spb}$.

At the end, the required pseudo-spectrum allows the estimation of the spectral content of the filtered phase signal.

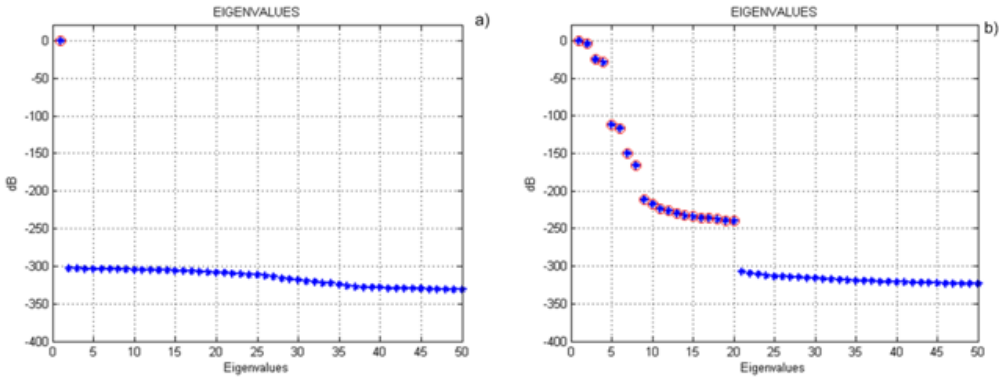

Figure 23: Eigenvalues before (a) and after (b) the adopted decorrelation procedures; only the eigenvalues characterized by highest value are chosen to select the signal subspace.

4.3.4. Signal subspace selection

The adopted smoothing procedure aims at increasing the dimension of the signal subspace in order to improve the robustness of the proposed method in actual measurement conditions. In the assumption of ideal conditions (i.e. evolution of the chest displacement versus time modeled as a pure sinusoidal tone), the signal subspace and the related matrix should still have rank equal to 1, also after the smoothing procedures, because the sub-arrays obtained from the phase signal segmentation are all dependent on one another, and the dimension of the space signal should not change.

In actual scenarios, the phase signal associated with the breathing turns out to be characterized by a not perfectly sinusoidal evolution versus time during the observation interval and, consequently, by a certain number of spectral components located around 0.3 Hz (typical value of the frequency of breathing).

This way, the sub-arrays obtained after the decorrelation procedures will not be all dependent on one another due to the effect of noise and a certain degree of

spectral dispersion. So, the rank of the matrix of the signal subspace should be at most equal to the number of the considered sub-arrays; it is worth noting that a lower number of eigenvalues is taken into account and considered significant, and the proposed strategies makes the eigenvalues selection more straightforward with respect to other solutions already presented in the literature [55]. In particular, the eigenvalues characterized by higher values and associated with spectral components very close to $0.3\,\text{Hz}$ are retained, thus allowing the adopted procedure to estimate the different spectral components involved in the received phase. To this aim, the most independent sub-arrays are selected by means of the rank of the adopted signal subspace. The remaining eigenvalues, related to differences due to the involved noise and showing the lowest values, are discarded. In particular, the eigenvalues whose normalized amplitude is below $-30\,\text{dB}$ are dropped.

As stated above, the chest displacement depends on two different contributions, related respectively to breathing and heartbeat, and characterized by different typical amplitudes. In particular, for body movements due to heartbeat, the amplitude is usually within the range of $0.05\,\text{mm}$ [31]; on the contrary, displacement associated with the respiration can be as large as several millimeters.

This way, the higher the number of considered eigenvalues in spectrum estimation, the richer will be the reconstruction of the spectral content. However, in order to improve the spectrum readability and, consequently, the detection of human beings, the signal subspace is selected in such a way as to filter out (*i*) low amplitude harmonics of breathing and (*ii*) tones associated with heartbeat.

For the sake of clarity, Fig.24 shows the spectra obtained by the proposed method when the rank of the signal subspace is increased from 5 up to 19; this way, more spectral components can be taken into account, to the detriment of certain amount of noise introduced in the signal subspace. As it can be seen, new peaks appear in the obtained spectrum; some of them (in particular, the one

centered at 1.25 Hz) should be associated with heartbeat, even though the presence of harmonics related to the breathing could give rise to false detection.

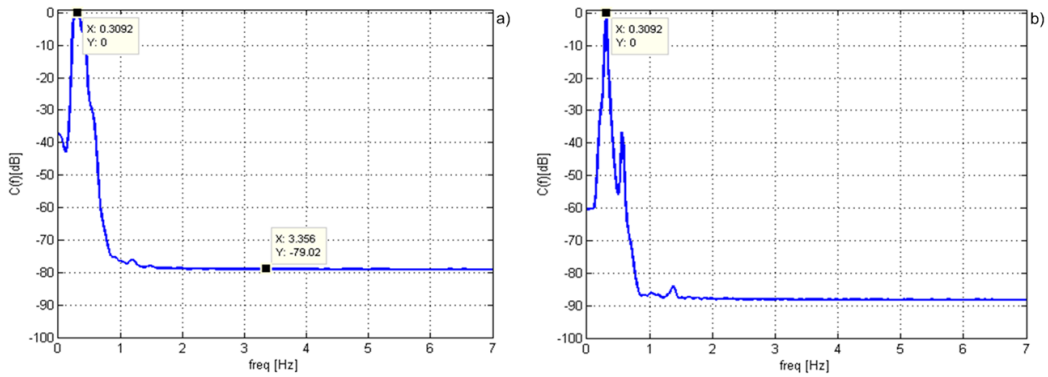

Figure 24: Pseudospectra obtained by means of the proposed method obtained by selecting signal subspaces of rank equal, respectively, to 5 and 19.

A procedure for automatic rank selection has been adopted, in particular, Aikake's information criterion (AIC) [56] allows determining the number of significant eigenvalues by means of a deterministic procedure to the detriment of a limited increase of computational burden. AIC belongs to a family of methods that use information theoretical criteria (ITC).

The basic idea is the identification, within a defined set of likelihood functions, of that which better represents the distribution of N observations of the same statistical process. In particular, the AIC method selects the likelihood function $LF\left(\mathbf{Z}\middle|\mathbf{p},k\right)$ that minimizes the expression

$$\mathrm{AIC}\left(\mathbf{Z}\middle|\mathbf{p},k\right)=-2\log\left(LF\left(\mathbf{Z}\middle|\mathbf{p}\right)\right)^{m-k}+2k\left(2m-k\right) \tag{4.24}$$

where k stands for the number of significant parameters in the statistical model, m is the whole number of parameters, $\mathbf{Z}$ is the actual (measured) covariance matrix, and $\mathbf{p}$ represents the constraints to be met for the minimization of the likelihood function. The pair $\left(\mathbf{p},k\right)$ minimizing eq. (4.24) has to be found; the

value of k provides the desired number of significant eigenvalues, [56]-[57]. It is worth noting that the constraints $\mathbf{p}$ can be expressed in terms of eigenvalues and eigenvectors of $\mathbf{Z}$, and, if the observations are linearly independent, the logarithm of the likelihood function computed from the covariance matrix can be expressed as

$$\log\left(LF\left(\mathbf{Z}|\mathbf{p}\right)\right) = -N\log\left(\det\left(\mathbf{Z}\right) - \mathbf{Z}^{H}\mathbf{Z}\right) \tag{4.25}$$

where $\mathbf{p} = \left\{\overline{\lambda_1},..,\overline{\lambda_m},\overline{\boldsymbol{\sigma}^2},\overline{u_1},...,\overline{u_m}\right\}$.

It is possible to demonstrate, as discussed in [58], that the logarithm of the likelihood function in eq. (4.25) is minimized if the constraints $\mathbf{p}$ are given by:

I. $\overline{\lambda_i} = \lambda_i$ with $i = 1,...,k$;

II. $\overline{\boldsymbol{\sigma}^2} = \dfrac{1}{m-k}\sum_{i=k+1}^{m}\lambda_i$;

III. $\overline{u_j} = u_j$, with $j = 1,...,m$.

Under these assumptions, eq. (4.24) can be rewritten as

$$\mathrm{AIC}\left(k\right) = -2\log\left(\frac{\prod_{i=k+1}^{m}\lambda_i}{\sigma^2}\right)^{m-k} + 2k(2m-k) \tag{4.26}$$

This way, the number of significant eigenvalues is given by the value d of the parameter k that minimizes the expression (4.26):

$$d = \min_{k=1,...,m} \mathbf{AIC}(k) \tag{4.27}$$

As an example, Fig.25 shows the results obtained by the proposed method when either threshold or AIC-based procedure is adopted for matrix rank

selection. Results refer to a scenario involving a human being located at a distance equal to *2 m* from the source and behind a brick wall *0.2 m* thick.

As it can be appreciated, adaptive rank selection assures a better resolution (sharper peak in the pseudospectrum) to the detriment of a slightly reduced dynamic range (DR). Since the aim of the method is the detection of vital signs, the adoption of threshold procedure should be advisable; moreover, reduced computational burden proves to be necessary for real-time operation, if needed. On the contrary, for very low signal-to-noise ratio (SNR), a more reliable procedure for rank selection, such as those involving AIC, should be preferable.

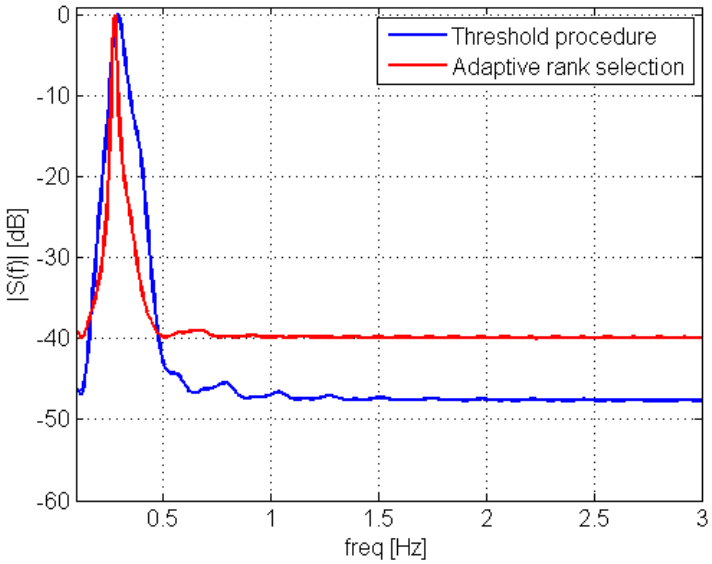

Figure 25: Comparison of the results obtained by the proposed method when threshold (blue line) or adaptive (red line) procedure are adopted for rank selection.

Chapter 5

Numerical results

In this Chapter the analysis of numerical results is performed in order to verify the behavior of proposed measurement methods in presence of noise. This Chapter is divided in two different sections, in the first one, the numerical results of measurement algorithm for through wall detection of moving target in different scenarios are shown and discussed, in particular a briefly description of adopted electromagnetic field simulator is provided and the obtained results in three different situations are presented. The block diagram of the cited method for TWI is sketched in Fig.9.

The second section is dedicated to Vital Signs Detection, a number of numerical tests are presented and discussed. All operating steps of Advanced Music Algorithm are shown in the block diagram of Fig.20. In particular, the dynamic range (DR) has been considered as performance factor. DR has been evaluated as the ratio of the amplitude of the spectral component mostly associated with breathing in the frequency range of interest to the amplitude of either the largest harmonic, spurious spectral component or noise floor.

5.1. Moving Target Detection

A number of tests have been conducted on numerically generated signals in order to preliminary assess the performance of the implemented procedures for moving target detection. An electromagnetic wave simulator based on FDTD

numerical method has been exploited to obtain scattered field synthetic data in different conditions.

5.1.1. GPRMAX

GprMax[4] is an electromagnetic wave simulator for Ground Penetrating Radar modeling. It is based on the Finite-Difference Time-Domain numerical method.

The FDTD approach to the numerical solution of Maxwell's equations is to discretize both the space and time continua. Thus the discretization spatial Δx, Δy and Δz and temporal Δt steps play a very significant role, since the smaller they are the closer the FDTD model is to a real representation of the problem.

However, the values of the discretization steps always have to be finite, since computers have a limited amount of storage and finite processing speed. Hence, the FDTD model represents a discretized version of the real problem and of limited size. The building block of this discretized FDTD grid is the Yee cell [59] named after Kane Yee who pioneered the FDTD method. This is illustrated for the 3D case in Fig.26a. The 2D FDTD cell is a simplification of the 3D one and is depicted in Fig.26b.

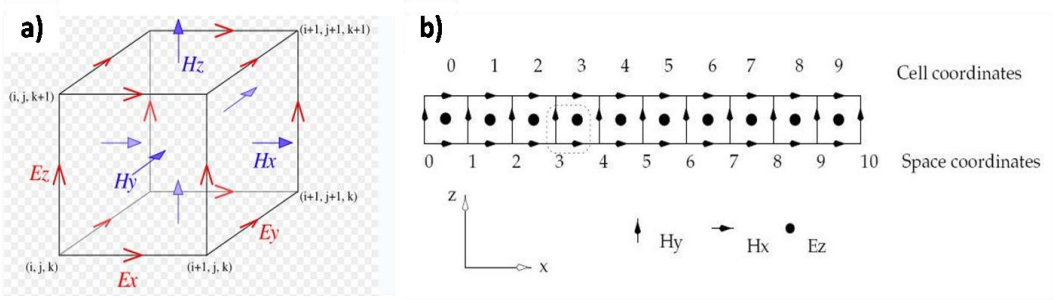

Figure 26: a) The 3D FDTD Yee cell; b) 2D FDTD cell

The numerical solution is obtained directly in the time domain by using a discretized version of Maxwell's curl equations which are applied in each FDTD

[4] www.gprmax.org

cell. Since these equations are discretized in both space and time the solution is obtained in an iterative fashion. In each iteration the electromagnetic fields advance (propagate) in the FDTD grid and each iteration corresponds to an elapsed simulated time of one Δt. Hence by specifying the number of iterations one can instruct the FDTD solver to simulate the fields for a given time window.

The price one has to pay of obtaining a solution directly in the time domain using the FDTD method is that the values of Δx, Δy, Δz and Δt cannot assigned independently. FDTD is a conditionally stable numerical process. The stability condition is known as the CFL condition after the initials of Courant, Freidrichs and Lewy and is

$$\Delta t \leq \frac{1}{c\sqrt{\frac{1}{(\Delta x)^2}+\frac{1}{(\Delta y)^2}+\frac{1}{(\Delta z)^2}}} \tag{5.1}$$

where c is the speed of light. Hence Δt is bounded by the values of Δx, Δy, Δz. The stability condition for the 2D case is easily obtained by letting $\Delta z \to \infty$.

One of the most challenging issues in modeling *open boundary* problems as the GPR one is the truncation of the computational domain at a finite distance from sources and targets where the values of the electromagnetic fields cannot be calculated directly by the numerical method applied inside the model. Hence, an approximate condition known as *absorbing boundary condition* (ABC) is applied at a sufficient distance from the source to truncate and therefore limit the computational space. The role of this ABC is to absorb any waves impinging on it, hence simulating an unbounded space. The computational space (i.e. the model) limited by the ABCs should contain all important features of the model such as sources and output points and targets.

In constructing a GPR model in two and three dimensions, some assumptions are necessary. The assumptions made for both GprMax2D and GprMax3D models are:

- all media are considered to be linear and isotropic.
- in GprMax3D if the physical structure of the GPR antenna is not included in the model then the antenna is modeled as an ideal Hertz dipole (i.e. a small current source). In GprMax2D the transmitting antenna is modeled as a line source.
- the constitutive parameters are, in most cases, assumed not to vary with frequency. This assumption simplifies a time domain model. However, a formulation able to handle a Drude (i.e. Debye plus a constant conductivity) relaxation model for the complex permittivity is included in both GprMax2D and GprMax3D.

Therefore, for the 2D case the governing equations reduce to the ones describing the propagation of *TM* mode electromagnetic waves.

The input file must contain:

- size of investigation domain;
- the discretization steps, Δx, Δy and Δz;
- observation time window;
- geometry of scenario (furniture, target);
- type of electromagnetic source and its excitation waveform.

The available choices for excitation waveform are:

- *cont_sine* which is a continuous sine waveform at the specified frequency. In order to avoid introducing noise in the calculation the waveform's amplitude is modulated for the first cycle of the sine wave (ramp excitation).
- *sine* which is a single cycle of a sine waveform at the specified frequency.
- *gaussian* which is a gaussian waveform;
- *ricker* which is the first derivative of the gaussian waveform:

$$I = -2\xi\sqrt{e^{\frac{1}{2\xi}}}e^{-\xi(t-\chi)^2}(t-\chi) \tag{5.2}$$

where $\xi = 2\pi^2 f^2$, $\chi = \frac{1}{f}$.

- *user* which can used to introduce into the model User defined excitation functions.

5.1.2. Numerical Test

The simulated measurement system consists of an uniform linear array of antennas operating according to a multi-monostatic approach, positioned at a distance equal to $0.3m$ from the first wall interface and illuminating a complex investigation domain of $15m^2$ ($3m \times 5m$). The elements of the array are arranged on the full length of $3m$; in particular, each element is separated from one another by $\frac{\lambda_{\min}}{2} = 0.125m$ and is characterized by a nominal frequency bandwidth from $(300 \div 1200)\,MHz$. The lower bound has been determined according to the size of antennas usually adopted in this kind of applications, while the upper bound has been set as the optimal trade-off between the required resolution and wall permeability to the radiation. With regard to the excitation waveform, a *Ricker* pulse has been adopted, whose center frequency has been stepped by $31\,MHz$ (i.e. 30 different frequencies in the considered bandwidth); the step value has been set according to the relationship in (3.8).

Finally, observation windows with a duration of $45\,ns$ have been considered, in order to cover the full depth of the investigation domain.

For each test, the thickness of the wall has been set to $0.2m$, its dielectric permittivity has been chosen equal to $\varepsilon_w = 3\varepsilon_0$) and the associated effective conductivity has been fixed to $\sigma_w = 0.01\ S/m$. As for the TSVD truncation index, it was chosen to retain the singular functions corresponding to the singular

values not lower than $20\,dB$ with respect to their maximum value. Different scenes have been taken into account. For each of them, the data of the scattered field have been evaluated through the electromagnetic simulator GprMax.

Scene 1

The simulated scene is shown in Fig.27. The investigation domain has included a wooden table ($\varepsilon_t = 3\varepsilon_0$), a sofa, and two cupboards. A person walking at a speed of about $0.8 m/s$ has been supposed to move towards the table. The obtained results are represented in Fig.28; in particular, the time sequence of the reconstructed snapshots before applying the threshold procedure is given. The moving target has been well localized in all the snapshots and, as expected, the adopted differential approach removed the stationary targets in the investigated domain. Moreover, the mutual interactions between the moving target and the stationary objects have given rise to spurious artifacts (see, for example, Fig.28c and Fig.28e).

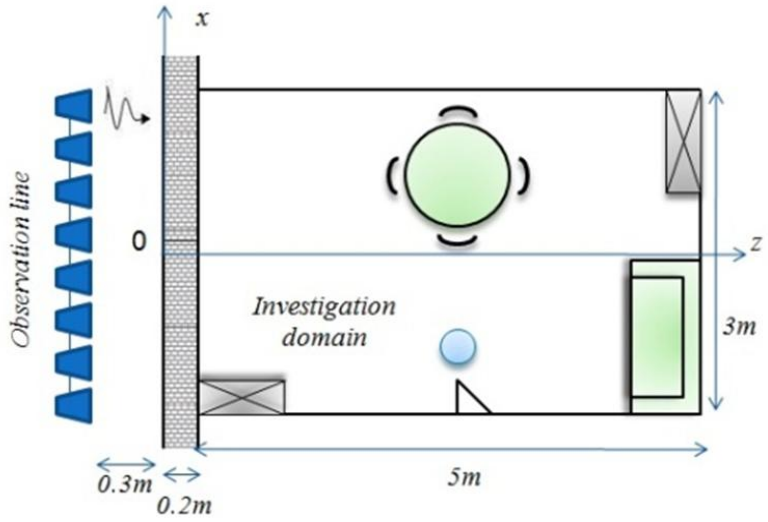

Figure 27: Geometric model of the room considered in Scene 1.

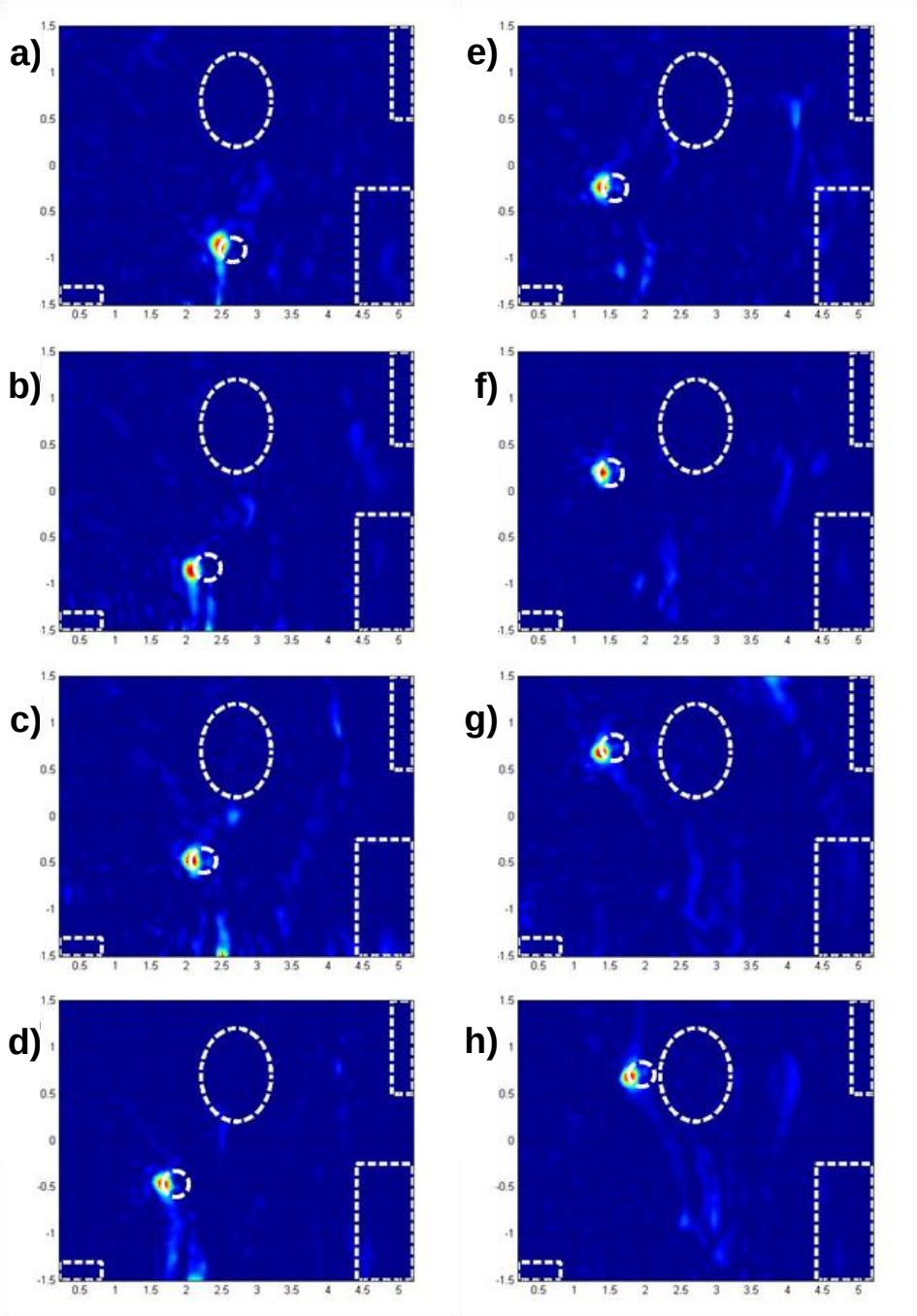

Figure 28: Some reconstructed images provided by the proposed method in Scene 1. The presentation order reflects their time evolution order. The dashed lines represent the stationary targets, while the full line circle specifies the nominal position of the modeled target.

In Fig.29, the results provided by the tracking algorithm are given; in particular, the position of the moving target in each time interval has automatically been extracted. As stated above, the presence of spurious artifacts, due to the furniture and not representative of the moving object, have been prevented through the threshold procedure; it is worth noting that the same threshold value (equal to $20\ \%$ of the maximum value of R_γ in the considered snapshot) has been adopted in all the conducted tests. It is possible to appreciate the remarkable agreement between the nominal (cross marker) and estimated positions (circle marker). For the sake of clarity, Table IV provides the distance between nominal and estimated position for each snapshot considered in Scene 1. An offset of about $0.12m$ can be noticed, mainly due to the adopted model of the target; more specifically, the method estimates the target position as that associated with its external edge, while the nominal position is associated with the target center.

The root mean square error (RMSE) on the position estimation has been considered as performance factor, defined as:

$$RMSE = \sqrt{\frac{1}{N}\sum_{i=1}^{N} d_i^2} \tag{5.3}$$

where N is the number of snapshots and d_i is the distance between nominal and estimated position (error). The RMSE in the first numerical test is equal to $0.103\ m$.

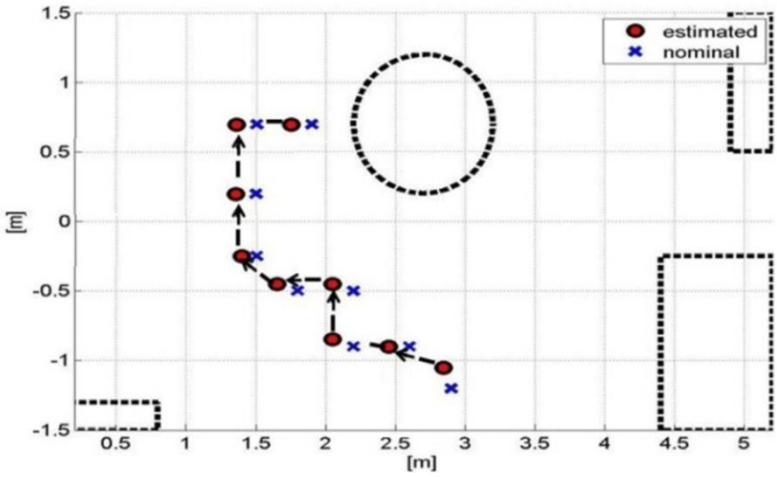

Figure 29: Result of the tracking algorithm in Scene 1. The circle is the moving target position provided by the proposed method, while the cross is the nominal position of the target center. The dashed lines represent the stationary targets.

Scene 2

In the second scene, shown in Fig.30, two bodies (target 1 and target 2) walking at speed of about $0.8 m/s$ in an empty room have been considered. In Fig.31 the time sequence of the reconstructed snapshots is given. The results of the tracking algorithm are given in Fig.32.

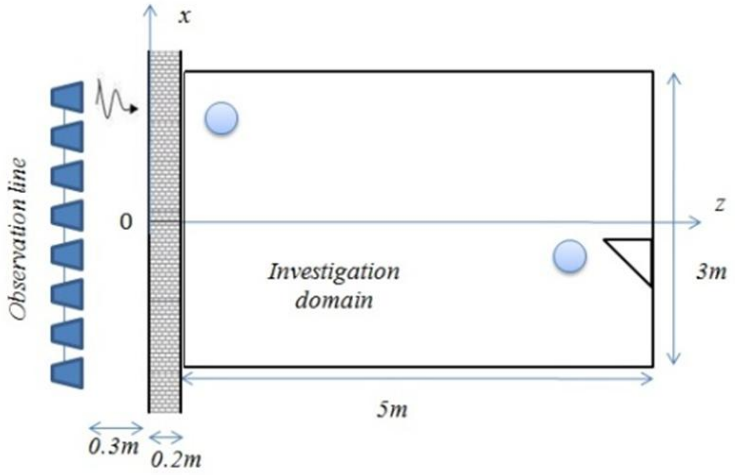

Figure 30: Geometric model of the room considered in Scene 2.

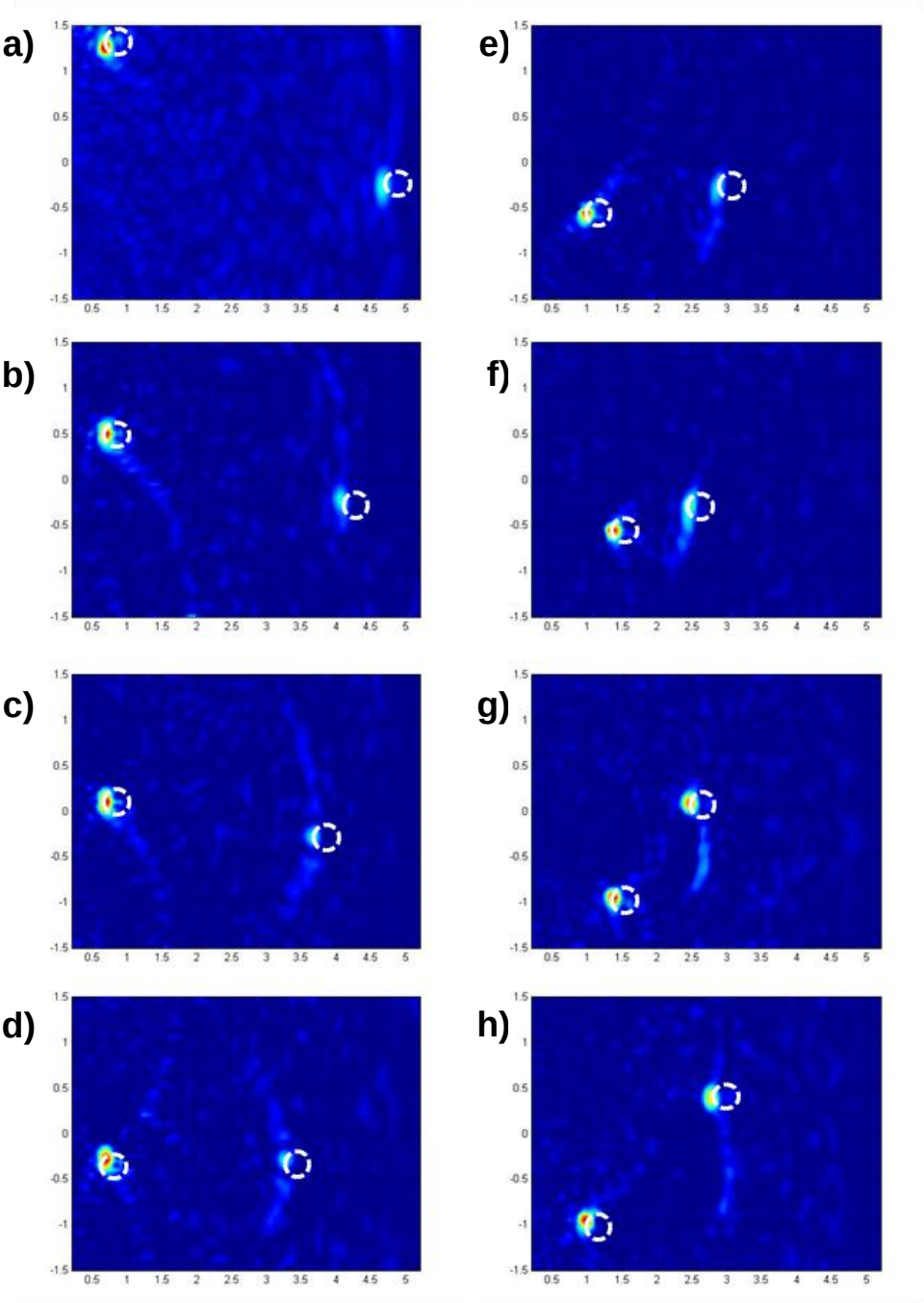

Figure 31: Reconstructed snapshots provided by the proposed method in Scene 2.

Spurious artifacts due to the mutual interactions between the moving targets can be noticed; as stated in §3.4, they do not give rise to false detection, being present

only in less than three consecutive snapshots. Also in this case, remarkable agreement between nominal and estimated positions has been experienced.

The distance between nominal and corresponding estimated positions is given in Table V. Also in the presence of two targets moving along different trajectories, the proposed method has succeeded in correctly locating their positions. The RMSE values related to target 1 and target 2 are equal to $0.108\ m$ and $0.113\ m$, respectively.

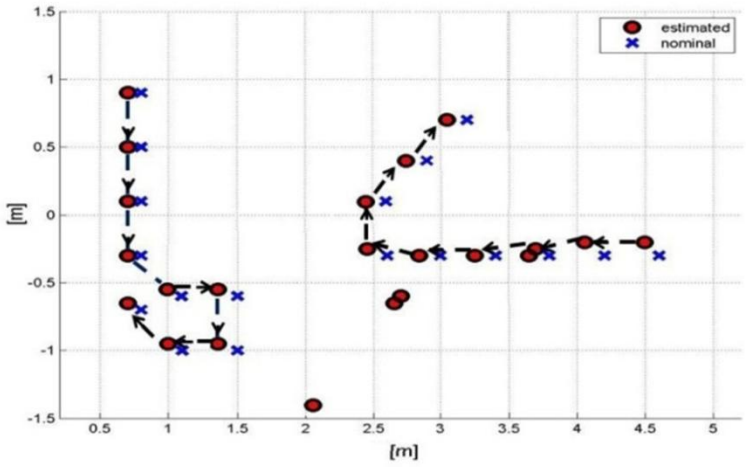

Figure 32: Result of the tracking algorithm in Scene 2.

Scene 3

The simulated scene, shown in Fig.33, has consisted of a cupboard and a sofa placed inside the investigation domain. Moreover, it has included two targets walking at a speed of about $0.8\ m/s$. Differently from the previous scenes, a noisy environment has been taken into account; in particular, the simulated data of the scattered field have been corrupted by Additive White Gaussian Noise (AWGN).

As an example, Fig.34 shows some reconstructed snapshots in the presence of a signal-to-noise-ratio (SNR) equal to 5 dB. In these frames, the presence of artifacts due to mutual interactions between the two targets is clearly evident. Nevertheless, the results of the tracking algorithm, given in Fig.35, highlight the efficacy of the

proposed method also in this critical condition. The position of both targets is correctly tracked, while the presence of spurious artifacts is almost completely removed thanks to the threshold procedure.

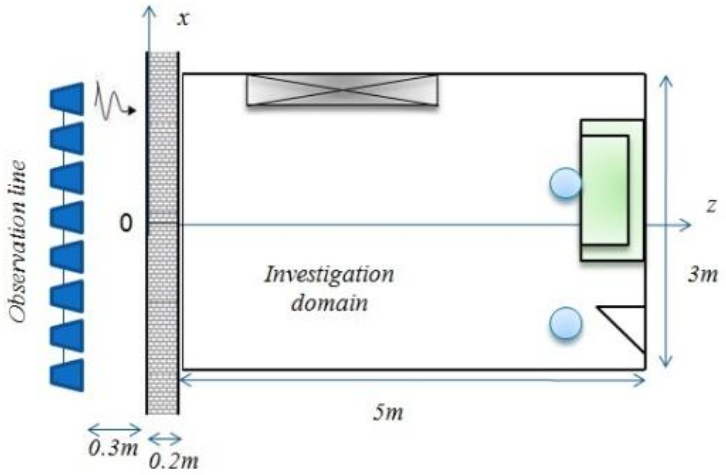

Figure 33: Geometric model of the room considered in Scene 3.

As shown in Table VI, the presence of noise slightly affects the overall performance of the method with respect to the ideal condition; the values of the distance between nominal and estimated positions of the targets have, in fact, been very close to those achieved in ideal conditions (no noise). The RMSE values related to target 1 and target 2 are equal to $0.101\ m$ and $0.100\ m$, respectively.

TABLE IV: DISTANCE BETWEEN NOMINAL AND ESTIMATED POSITIONS OF THE TARGET IN SCENE 1.

Position	*Distance (m)*
1	0.112
2	0.109
3	0.112
4	0.105
5	0.111
6	0.073
7	0.102
8	0.102
9	0.101
10	0.101
RSME	**0.103**

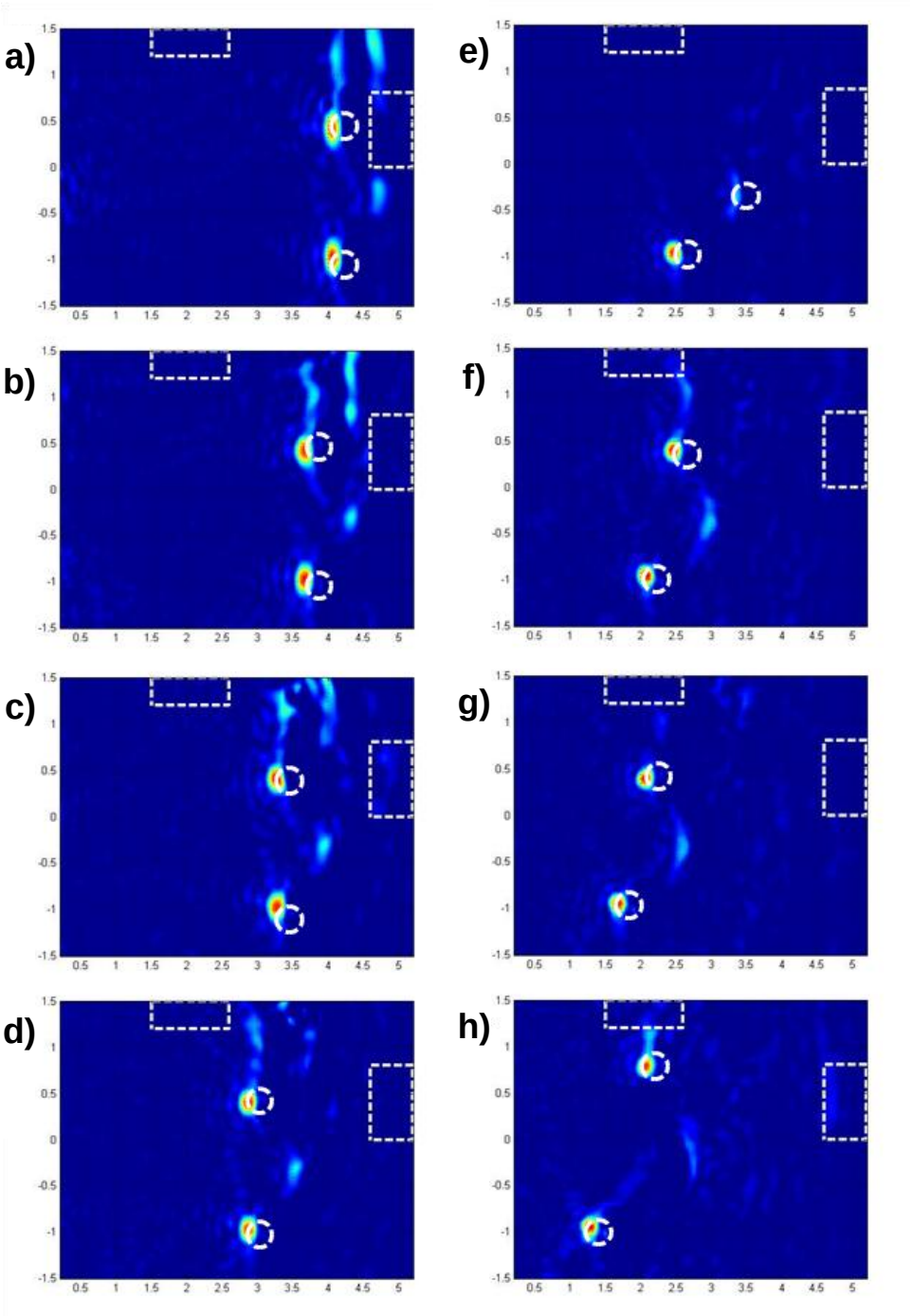

Figure 34: Reconstructed snapshots provided by the proposed method in Scene 3.

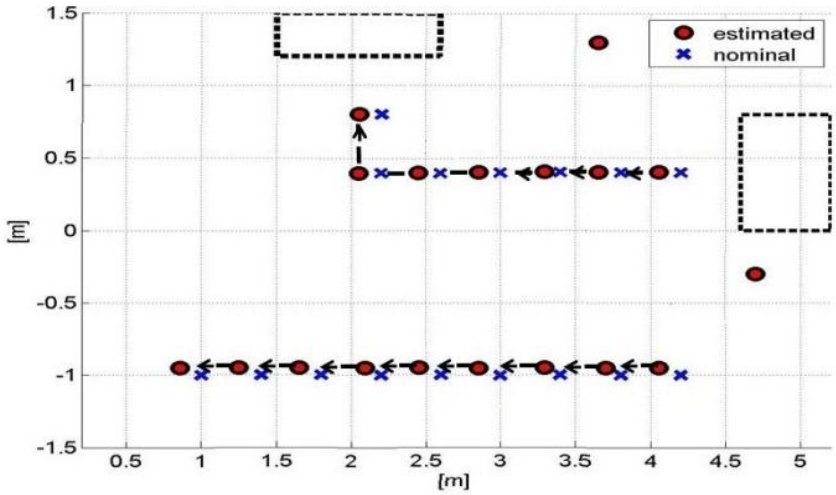

Figure 35: Results provided by the proposed method in Scene 3. The circle marker indicates the estimated moving target position. The cross marks the nominal position of the center of the targets.

TABLE V: DISTANCE BETWEEN NOMINAL AND ESTIMATED POSITION OF THE TARGETS IN SCENE 2.

Position	*Distance target 1 (m)*	*Distance target 2 (m)*
1	0.098	0.098
2	0.106	0.106
3	0.107	0.107
4	0.096	0.096
5	0.104	0.104
6	0.098	0.098
7	0.098	0.098
8	0.096	0.096
9	0.099	0.099
RSME	**0.108**	**0.113**

TABLE VI: DISTANCE BETWEEN NOMINAL AND ESTIMATED POSITION OF THE TARGETS IN SCENE 3.

Position	*Distance target 1 (m)*	*Distance target 2 (m)*
1	0,109	0,104
2	0,115	0,105
3	0,084	0,072
4	0,112	0,102
5	0,113	0,102
6	0,088	0,103
7	0,083	0,104
8	0,111	0,104
9	0,085	0,104
RSME	**0.101**	**0.100**

5.2. Vital Signs Detection

Preliminary numerical tests have been carried out in order to assess the algorithm performances in presence of noise. A sinusoidal signal, that represents the chest movement, has been corrupted by different levels of noise and processed with different techniques.

5.2.1. Numerical Test

The signal model for numerical assessment has been described in §4.1, the chest movement is modeled as the sum of two sinusoidal components related to breathing and heartbeat. The considered frequencies for breathing and heartbeat are $0.3Hz$ and $1.2Hz$.

The signal numerically generated has been corrupted by AWGN to simulate realistic operational conditions. In the first test, a signal to noise ratio (SNR) of $0dB$ has been considered. Fig.36 shows the evolution of the breath-filtered phase signal versus time along with its Discrete time Fourier Transform (DFT), while

the associated numerical results obtained by means of the Advanced Music are shown in Fig.37, it is evident the presence of vital signs spectral components.

In the second test the considered SNR is around $-10dB$, Fig.38 and Fig.39 show the obtained results. Also in this noise condition, the method works with success and the frequency components of interest are clearly detected while in DFT results many spectral components are evident.

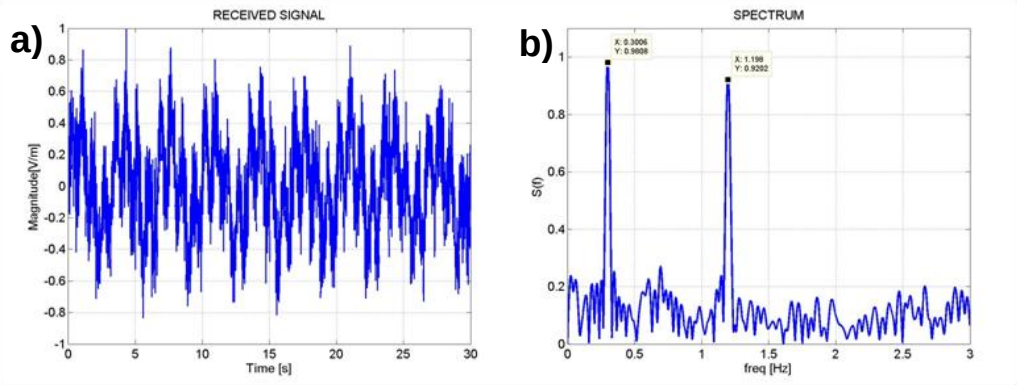

Figure 36: Filtered phase (a) evolution versus time and its amplitude spectrum (b) obtained by means of a traditional DFT algorithm in Test 1.

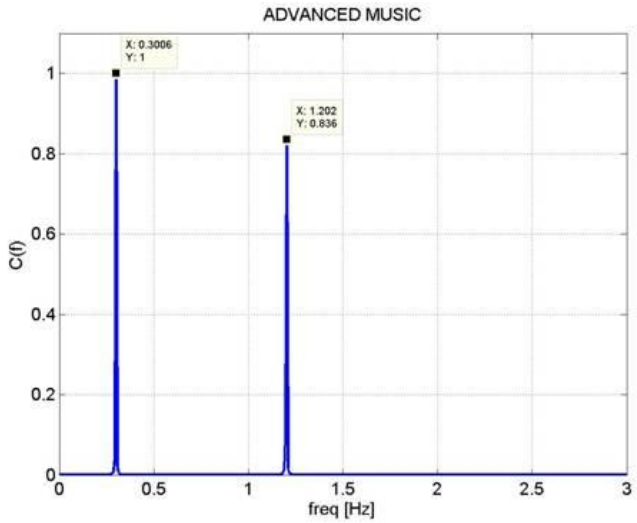

Figure 37: Results obtained by applying the Advanced Music in Test 1

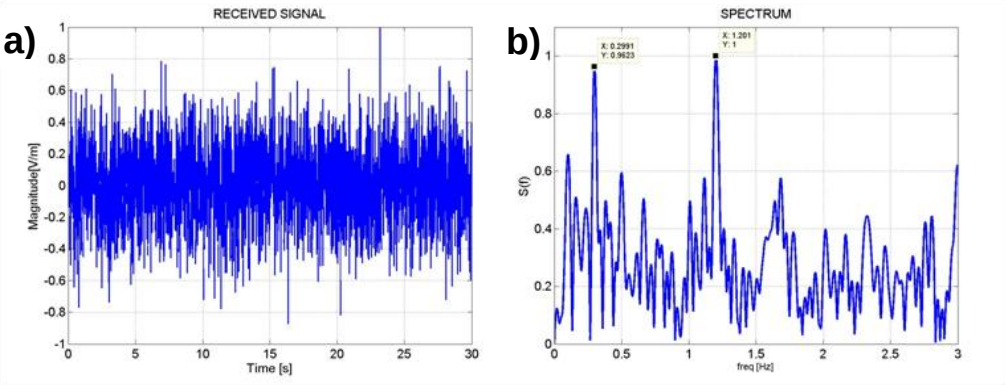

Figure 38: Filtered phase (a) evolution versus time and its amplitude spectrum (b) obtained by means of a traditional DFT algorithm in Test 2.

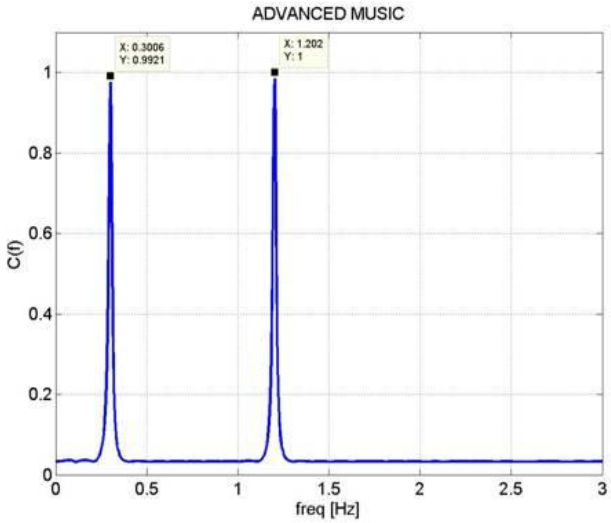

Figure 39: Results obtained by applying the Advanced Music in Test 2

5.2.2. Dynamic Range

The evolution of the obtained DR versus typical parameters such as SNR, amplitude of the chest displacements (DA) and observation interval (OI) has been estimated. In particular, numerical sinusoidal phase signal, characterized by a frequency equal to *2 Hz*, has been generated with a sampling rate equal to *50 Hz* and 20 values of DR have been estimated in different conditions of noise and phase amplitude for two different values OI (5 s and 10 s). Stemming from these

values, the surfaces of averaged DR and related experimental standard deviation σ_{DR} have been evaluated upon the varying of SNR and DA in the interval equal to $[-20 \div 20]dB$ and $[0.1 \div 10]mm$, respectively. The considered values of SNR has been chosen in order to simulate different (*i*) conditions of noise, (*ii*) wall thicknesses and (*iii*) distances between human target and radiofrequency source; on the contrary, the values of chest displacement range from shallow to panting breathing.

From the obtained results, shown in Fig.40 and Fig.41, some considerations can be drawn:

- the method provides satisfactory values both of DR and σ_{DR} but in very critical noise conditions;
- as it can be expected, the estimates of DR get better for increasing values of OI; a mean improvement of about 15 dB has been encountered;
- also in the presence of very limited chest displacement the method is capable of assuring reliable detections provided that a suitable OI is granted.

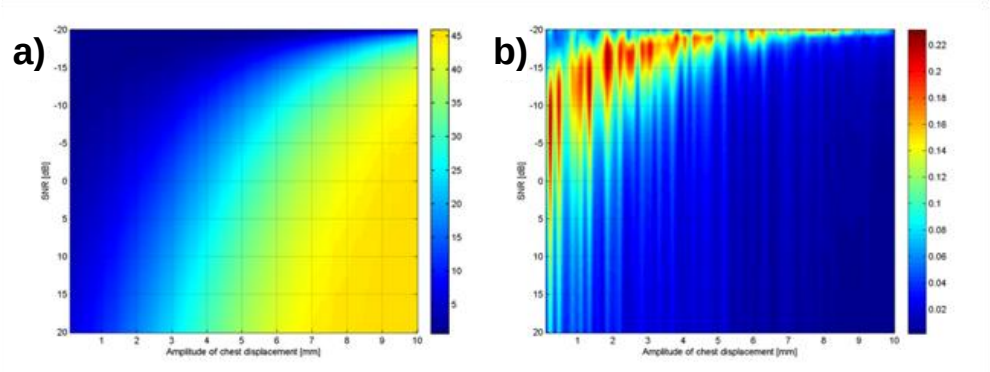

Figure 40: Evolution versus SNR and chest displacement of DR (a) and σ_{DR} (b) (expressed in relative terms) obtained for an observation interval equal to 5s.

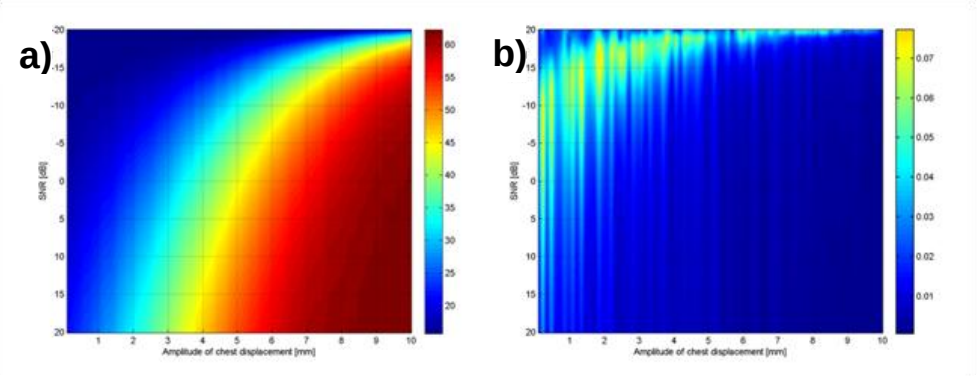

Figure 41: Evolution versus SNR and chest displacement of DR (a) and σ_{DR} (b) (expressed in relative terms) obtained for an observation interval equal to 10s.

5.2.3. Comparative analysis

To assess the performance of the proposed measurement method, Advanced Music, its numerical results have been compared to those gained by means of the other traditional techniques for Doppler frequency estimation, such as those based on Discrete Time Fourier (DFT) transform, maximum correlation algorithm [34], or a typical reconstruction method [47] exploiting singular value decomposition (SVD). With regard to the SVD-based method, the same adaptive rank selection described in §4.3.4 has been used. As an example, a new scenario, involving a human being located at a distance equal to $2\,m$ from a brick wall $0.2\,m$ thick, has been taken into account.

The results of the comparison are given in logarithmic scale, Fig.42, where the superior performances of the Advanced Music are clearly evident. In particular, the new method assures better performance in terms of achieved dynamic range with respect to the other considered methods, thus assuring a suitable noise rejection in whole analyzed frequency interval. Table VII gives the values of DR for the considered scenario; the outstanding performance of the Advanced Music can be appreciated. Moreover, differently from SVD and DFT-based approaches, the obtained spectrum appears free from spurious peaks that can be accidently associated with actual frequency components of the input signal.

Furthermore, the Advanced Music allows extracting the required information on target frequency with an acquisition time significantly lower than that needed by the other techniques. Finally, remarkable advantages are obtained also in terms of computational burden; the adopted decorrelation strategy makes, in fact, the new method capable of providing its results in few seconds, with a significant reduction with respect to the other considered methods.

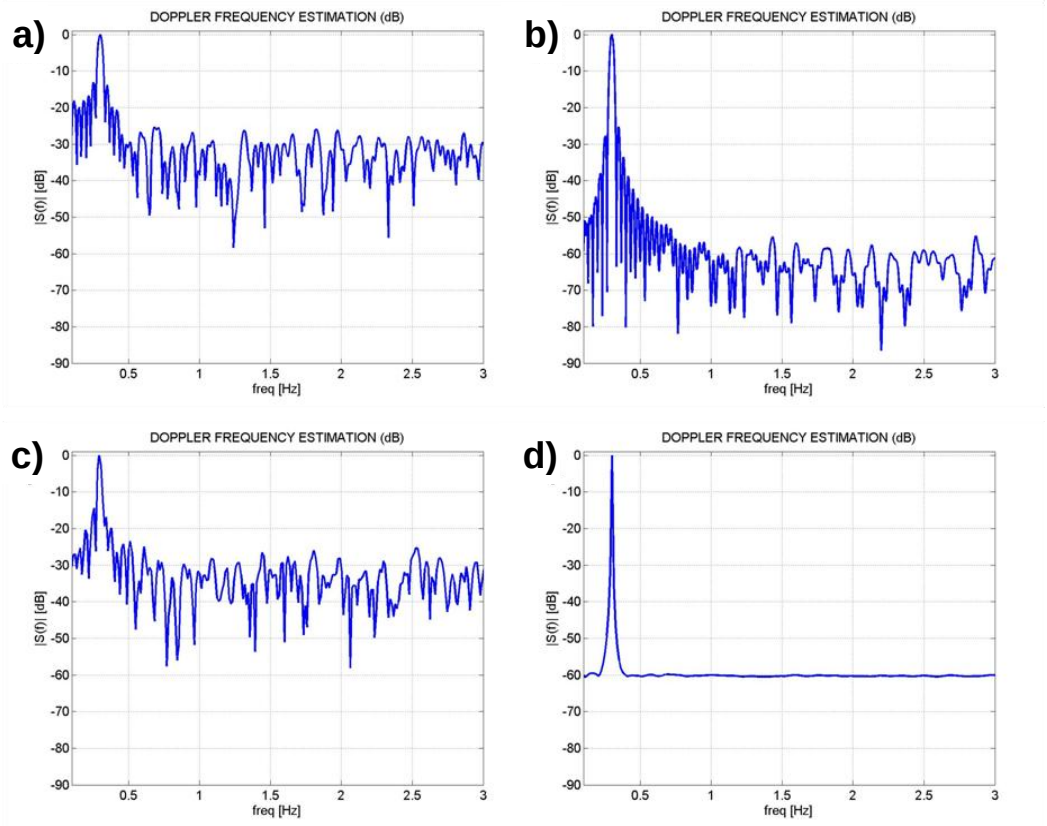

Figure 42: Comparison of results obtained by means of Advanced Music and those granted by other literature solutions in logarithmic scale. a) DFT, b) Max Correlation, c) SVD, d) Advanced Music.

TABLE VII: DR ACHIEVED THROUGH THE PROPOSED AND OTHER CONSIDERED METHODS.

Method	*Dynamic Range (dB)*
DFT	13 *dB*
Max Correlation	25 *dB*
SVD	14.5 *dB*
Advanced Music	**60 *dB***

Chapter 6

Experimental Validation

In this Chapter, the previously presented simulation procedures have been applied to the measured data collected in different experiments. The structure is similar to that of the previous chapter, it presents two sections: the first one describes the instrumentation and shows the experimental results of the application of proposed method for Through Wall Detection of moving target; the second one provides a description of measurement station, the adopted instrumentation and a discussion of obtained experimental results in the Vital Signs Detection.

6.1 Moving Target Detection

Several tests have been performed in order to assess the robustness of the proposed method in Chapter 3 with regard both to model errors and actual measurement noise as well as highlight the reliability of its results.

In the first section is introduced and described the prototype of Through Wall Radar adopted for experiments, in the second section a detailed description of considered scenarios and experimental results is provided.

6.1.1 Through Wall Radar

A prototype of the measurement system realized by Ingegneria dei Sistemi (IDS) S.p.A. has been adopted for experiments, Fig.43.

The Through Wall Radar (TWR) operating in S band exploits the multistatic/multiview approach. The S band is a good compromise between wall penetration capabilities, signal amplitude, resolution and Doppler.

The radar consists of uniform linear array of antennas (each of which operating both as transmitter and receiver) arranged on different lines and spaced by $\lambda_0/2$, where λ_0 is the wavelength associated with the center frequency of the considered band. The sensor geometrical arrangement reflects the typical radar architecture, based on a triangular structure for each channel to transmit and receive. The arrangement on two lines allows simplifying the complexity of the feeding network of the system, but introduces a model error as a consequence of the considered two-dimensional geometry (cut at constant quote). For this reason, an appropriate compensation procedure, based on a simple phase correction of the received signals, has been adopted.

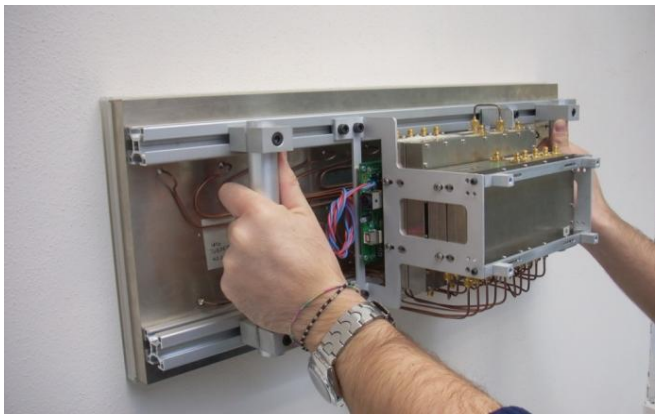

Figure 43: Prototype of Through Wall Radar adopted for experiments (Courtesy of IDS S.p.A)

The prototype operates as a Stepped Frequency Continuous Wave (SF-CW) sensor with a fractional bandwidth equal to 0.227 (defined as $\frac{f_{\max} - f_{\min}}{f_0}$, where f_0 is the center frequency).

SF-CW radar transmits a sequential series of individual frequencies whose amplitude and phase are accurately known, in particular it incorporates successive transmission of N sinusoids separated in frequency by Δf Hz. At each frequency the backscattered signals are received and fed to a mixer via a low noise amplifier (LNA). An IF filter is implemented in order to filter out-of-band noise. The bandwidth of the IF filter is thus proportional to the overall dynamic range (by varying the noise floor), but inversely proportional to the acquisition time. This is trade-off and it is a subject of optimization, depending on application, in fact with respect to pulsed systems, SF-CW technology assures a better SNR to the detriment of the acquisition time.

All antennas included in the upper line act as transmitting antennas while those included in the lower line are used as receiving antennas. In particular, when a specific antenna of the upper line is transmitting its electromagnetic signal, the two dipoles of the lower line surrounding the transmitting antenna are active. As an example, when the dipole TX_1 of Fig.44 works as a transmitter, RX_1 and RX_2 receive the scattered field.

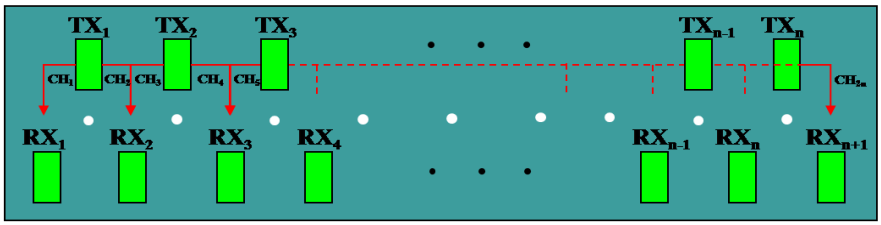

Figure 44: Fig.11 Geometric scheme of the prototype (Courtesy of IDS S.p.A.).

Before the execution of the experiments, the prototype has been suitably calibrated in order to remove the systematic errors due to radar circuitry, cables, and cable-antenna connections. The scattered field can, then, be obtained from actual measurements concerning the scattering parameter S21. As far as the radar system is concerned, the system includes a phase auto-calibration circuit to compensate possible differences in the internal circuitry. In particular, the calibration process is completely automated and repeated at defined time instants during the measurements, thus allowing the effect of system thermal drift to be tracked and corrected.

6.1.2 Experiments

In the experimental validation a large number of experiments have been carried out in order to assess the performance of the proposed method. In the following interesting experiments exploiting a first prototype of the TWR are discussed.

In the experiments two different scenarios have been considered, in the first one the frontal wall thickness is about $0.2\,m$, it is composed by a cement layer with a thickness $d_1 = 0.05\,m$, two wire nettings separated by an air layer with thickness $d_2 = 0.1\,m$, and a last cement layer with $d_3 = d_1$, while the other external walls have a thickness equal to about $0.1\,m$. The investigation domain has consisted of a single rectangular room covering an area of about $60\,m^2$, Fig.45. In the second scenario an investigation domain of about $30\,m^2$ $(6m \times 5m)$ has been considered, within the domain are present several stationary targets. The wall is composed by bricks and its thickness is equal to $0.3\,m$.

With reference to the conducted experiments, the prototype has been placed against the wall, and different number of targets moving according to different trajectories has been considered. For sake of clarity, Scene 1 and Scene 2 refer to the first scenario, while the last experiment is related to the second scenario.

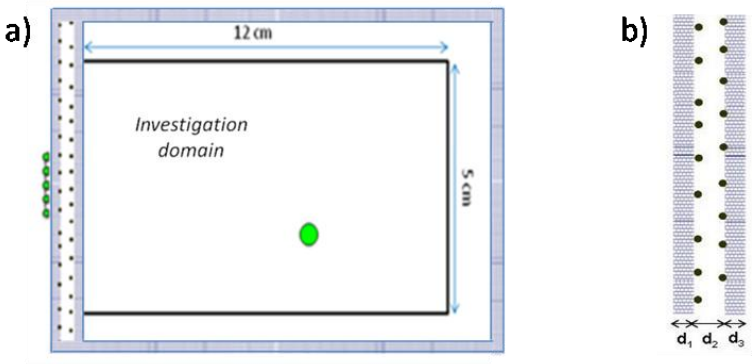

Figure 45: a) Geometric model of the room considered in the Scene 1 and Scene 2 b) Geometrical model of the wall.

Scene 1

The actual experimental set-up is shown in Fig.46. As a first example, a single man moves according to a zig-zag trajectory (i.e. a trajectory characterized by several short sharp turns) within the room.

Figure 46: Measurement set-up

Some snapshots provided by the method, after the application of the threshold procedure, are given in Fig.47, while the results of the automatic tracking algorithm are presented in Fig.48. Apart from some artifacts, the position of the

target has clearly been singled out and tracked. The nominal positions of the target have been estimated by setting a specific path on the ground with suitable markers, measuring their distance from two orthogonal walls and letting the target wait on each marker at least for the duration of the imaging procedure. The RMSE between nominal and estimated position is equal to 0.143 *m*.

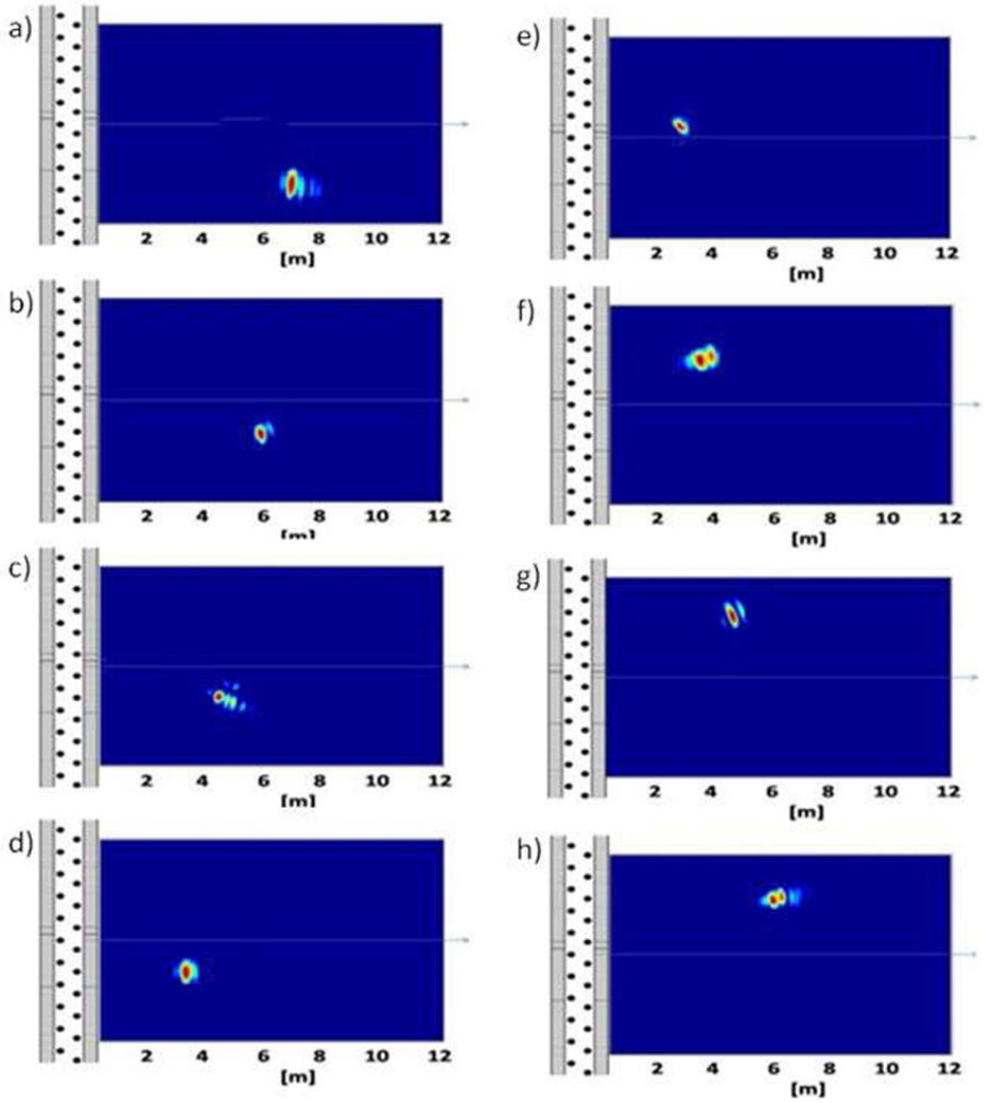

Figure 47: Snapshots provided by the proposed method in actual experimental tests involving a single moving target.

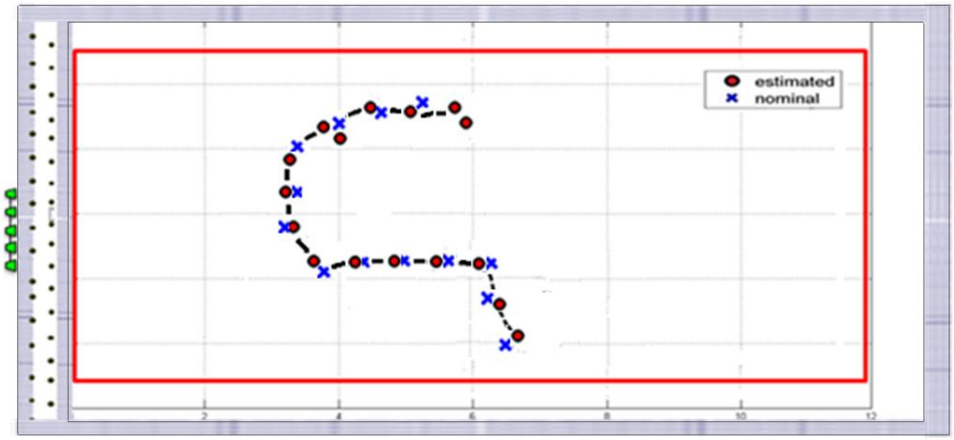

Figure 48: Results provided by the proposed method in actual experiments involving one moving target. The circle marker indicates the estimated moving target position. The cross marks the nominal position occupied by the target.

Scene 2

A second example has involved two targets moving within the same investigation domain, and whose trajectories have been characterized by an intersection. Some snapshots provided by the proposed method are given in Fig.49. As expected, the simultaneous presence of two targets has increased the presence of artifacts, mainly due to the scattering model errors associated with the layered structure of the wall (assumed as homogeneous), and whose effects have drastically been mitigated through the use of the threshold procedure (Fig.50). It is worth stressing that the method has succeeded in correctly estimating the position of the targets also in the presence of a layered wall, thus confirming its robustness.

The RMSE values related to target 1 and target 2 are equal to *0.145 m* and *0.163 m* , respectively .

Moreover, the adopted measurement station has proved very effective in terms of imaging rate (as high as 40 snapshots per second) and, consequently, appropriate for applications of real-time detection and tracking of human targets moving in two-dimensional scenes.

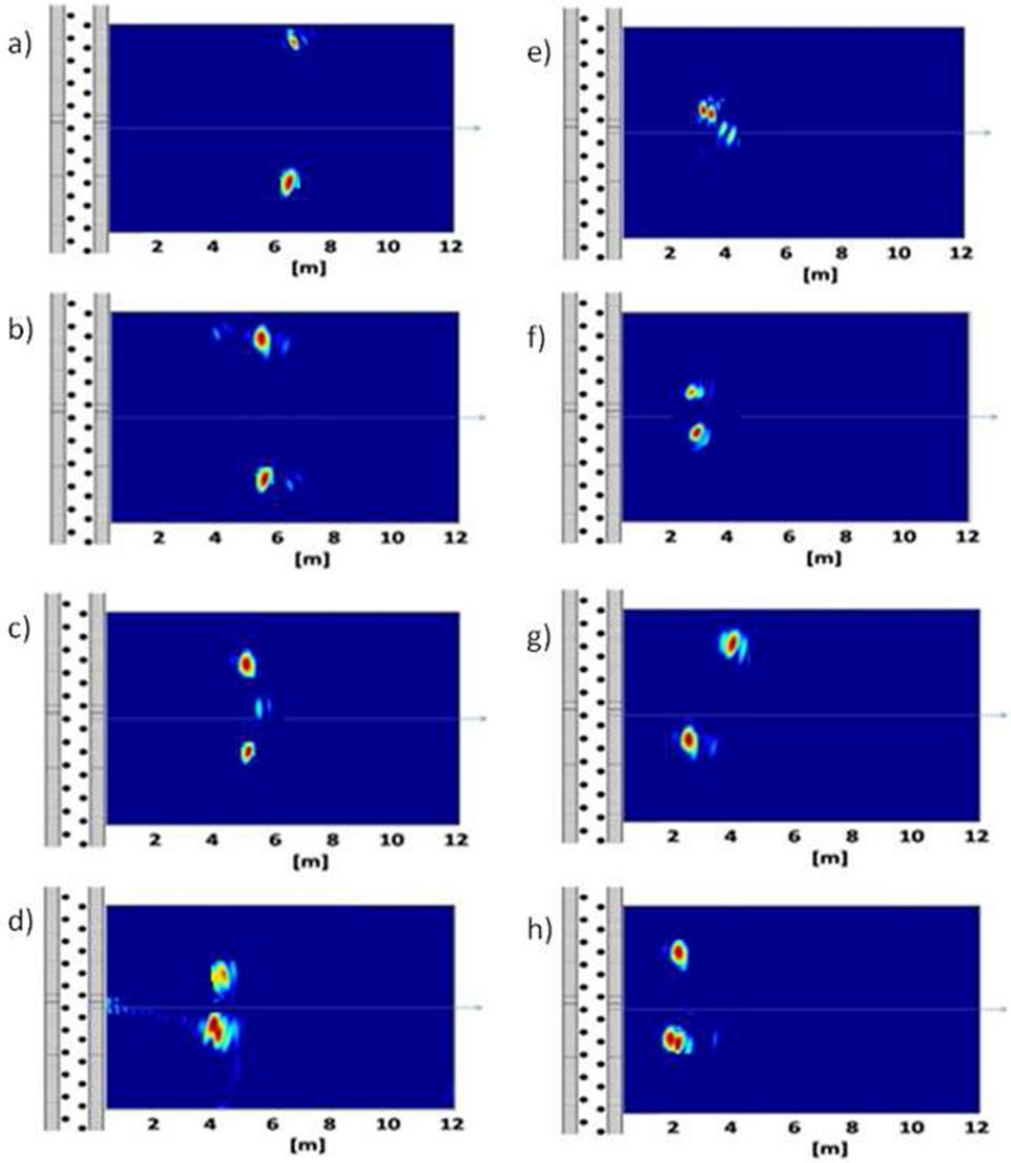

Figure 49: Snapshots provided by the proposed method in actual experimental tests involving a two moving targets.

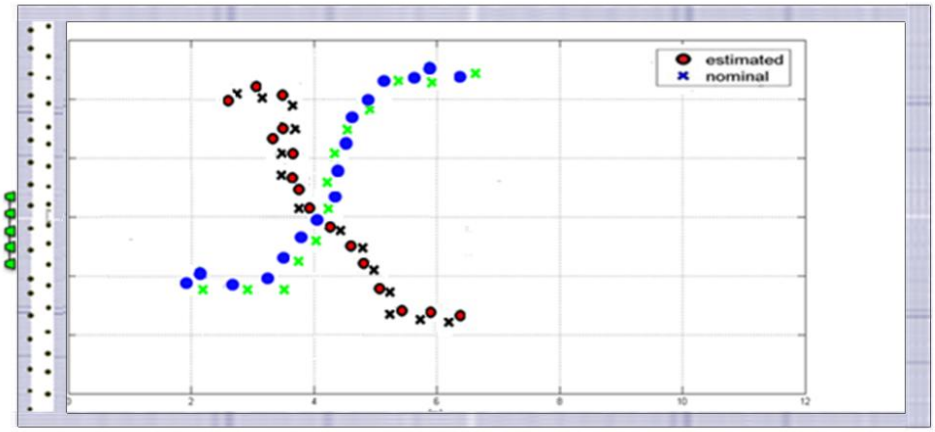

Figure 50: Results provided by the proposed method in actual experiments involving two moving targets. The circle marker indicates the estimated moving target position. The cross marks the nominal position occupied by the target.

Scene 3

The second scenario adopted for the experiments and the experimental set-up are shown in Fig.51. In the considered example, a single man moves within the investigation domain in presence of static objects. The TWR has been placed behind the wall shown in Fig.51.

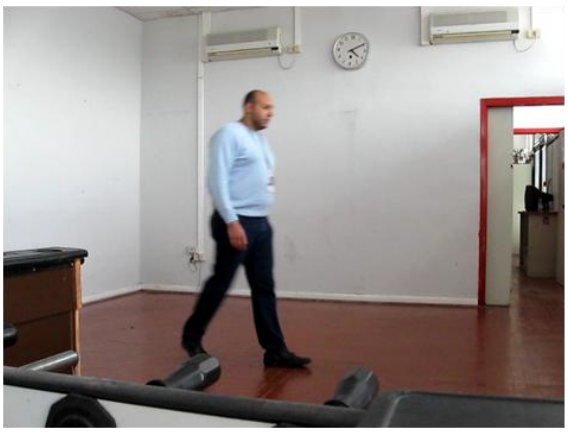

Figure 51: Considered scenario in experiments (scene 3).

In Fig.52 the results of the automatic tracking algorithm are presented, thanks to the MTI filter and the tracking procedure artifacts related to the interactions between the moving and static target do not appear, determining a correct estimate of the target position in the considered experiment.

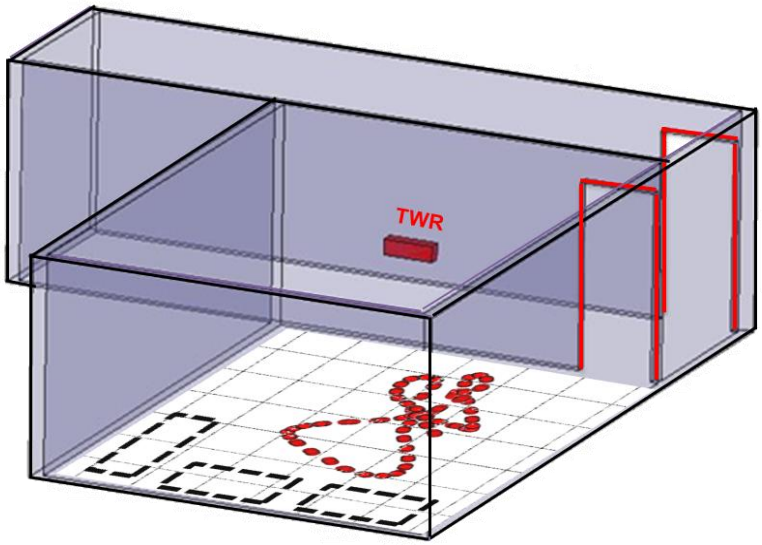

Figure 52: Results of the automatic tracking algorithm in presence of static targets.

6.2 Life Signs Detection

This section is devoted to the description and discussion of the experimental results obtained by proposed measurement algorithm for the life signs detection. Different configurations and people have been considered in the tests, highlighting the detection capability of the spectral component associated to breathing, and showing its good performance and robustness.

6.2.1 Measurement station

The measurement set-up along with the reference scenario adopted to assess the performance of the method is depicted in Fig.53. It consists of a microwave

coherent transceiver generating a sine wave whose carrier frequency is equal to 10 GHz; in particular, a network analyzer, namely E8362BTM by Agilent Technologies (receiver noise floor equal to $-123\,dBm$, $1\,Hz$ frequency resolution), has acted as a transceiver.

The two sensors are two traditional horn antennas, each of which characterized by a free space gain equal to $12\,dB$ in the frequency range of interest. The power of the transmitted signal is equal to $5\,dBm$. The receiver detects the in-phase (I) and quadrature (Q) components of the backscattered signal, which can be represented in the $I-Q$ plane as a complex phasor, the amplitude and phase of which vary according to the displacements of the human chest due to breath and heartbeat. The amplitude of the considered displacement is roughly a fraction of the wavelength characterizing the radiofrequency signals usually exploited.

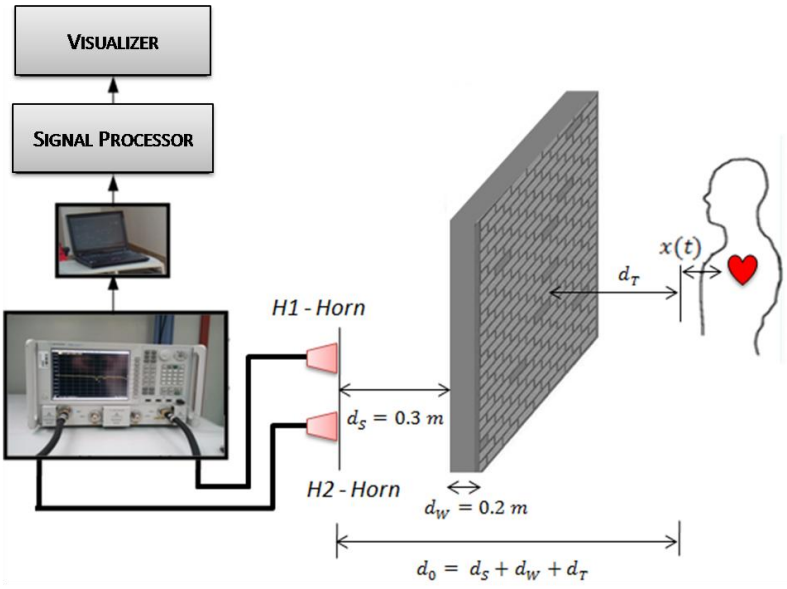

Figure 53: Measurement station for tests conducted in actual experimental tests.

The adopted frequency of $10\,GHz$ proves to be the right trade-off between the penetration depth through concrete walls (requiring low frequency radiations) and phase shift detectability due to breathing (which improves with higher

frequencies). In [60] is shown the RF attenuation for different types of walls; the worst case is concrete wall but the attenuation is still rather low and is less than $14\,dB$ for frequencies below $10\,GHz$. Finally, signals at $10\,GHz$ do not need a specific license.

According to the scheme reported in Fig.53, the signal is first transmitted by the horn referred to as *H1*, reflected by the obstacle and, finally, received by the horn referred to as *H2*. I and Q components of the received signal are digitized with a nominal sample rate of $1\,kSample/s$ and a memory depth equal to $16\,kSamples$. The obtained samples are transferred to a processing and control unit where the processing steps characterizing the new method are executed. It is worth noting that the measurement system needs a phase coherent condition, assured through the use of the PNA as a transceiver. With regard to the wall, its characteristics have been chosen according to their typical actual values; in particular, a *20cm*-thick wall, made of common brick, has been adopted. It is worth noting that, if the wall characteristics changes (as an example larger thickness or presence of metallic reinforcement), different values of carrier frequency should be adopted; the step of the method as well as its performance will not be affected.

6.2.2 Experiments

To assess the performance of the proposed method, a number of tests have been carried in a furnished room at the microwave laboratories of SELEX Electronics Systems.

As a first example, the results obtained when a standing person has been inside the furnished room at a distance $1\,m$ from the wall, are given. In particular, Fig.54 shows the evolution of the breath-filtered phase signal versus time along with its Discrete Time Fourier transform. A suitable procedure for the compensation of motionless targets contributes allows identifying the presence of

a periodic source behind the wall. Of course, from the analysis of Fig.54, it is very difficult to associate a human nature with the experienced periodic source. On the other hand, the received signal could give the opportunity of attaining such information, distinguishing between a human and a different periodic signal source.

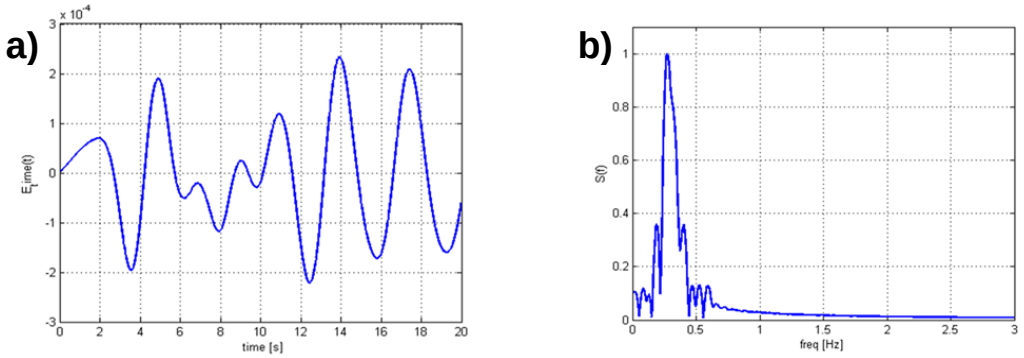

Figure 54: Filtered phase (a) evolution versus time and its amplitude spectrum (b) obtained by means of a traditional DFT algorithm.

Fig.55 shows the results obtained by applying the implemented method on a portion of the phase signal with time duration $T_S = 4s$, i.e. with an observation interval whose duration is very close to that of a single breathing period.

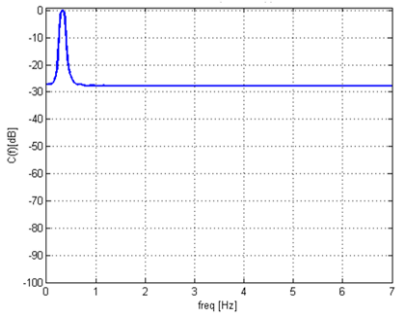

Figure 55: Results obtained by applying the traditional MUSIC algorithm on a single period of the filtered phase signal in logarithmic scale.

The performance of the implemented measurement algorithm in extracting the desired information about the spectral content of the filtered phase signal can be

appreciated in Fig.56, wherein the human nature of the periodic source can be easily detected. In particular, the representation of the pseudospectrum along a logarithmic scale (Fig.56b) highlights the large achieved dynamic range (about $70\ dB$), a very advisable issue for clutter rejection.

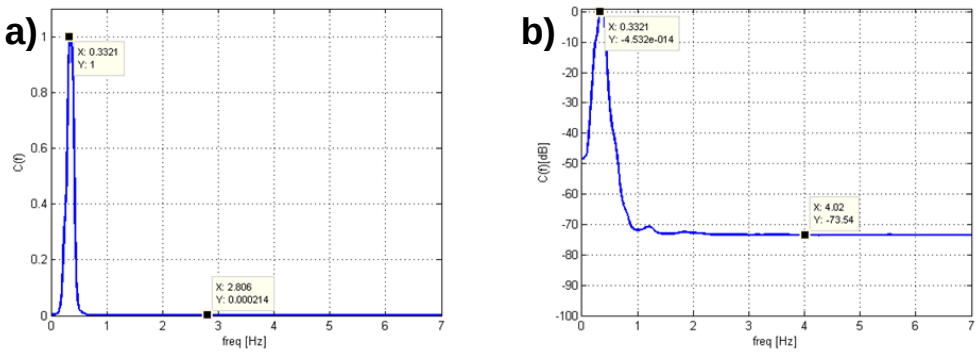

Figure 56: Results obtained Advanced MUSIC in the first test in (a) linear and (b) logarithmic scale.

As a second example, the results obtained when the method is applied to the signal related to a person holding his breath for a certain period of time at a distance $1\ m$ from the wall, are presented. In particular, Fig.57 shows the evolution of the phase signal versus time and its Discrete Time Fourier transform.

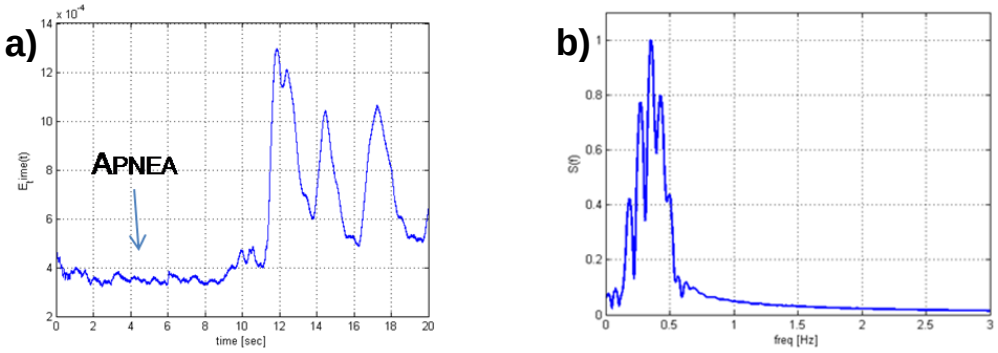

Figure 57: Evolution versus time (a) and its DFT (b).

Also in this case, the method works with success and the frequency component of interest is clearly detected. Fig.58 shows the excellent results obtained. The

breathing of the target can clearly be singled out, noise floor is at about $-70\ dB$, granting also in this measurement condition a large dynamic range and associated clutter rejection.

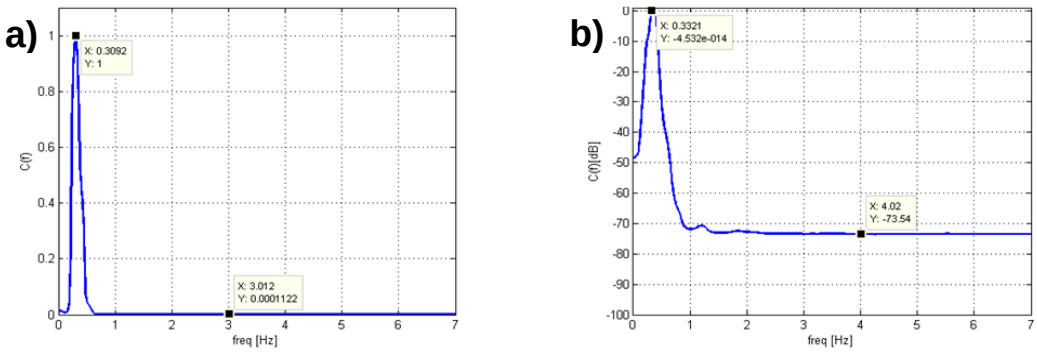

Figure 58: Results obtained by Advanced MUSIC in the second test in a) linear and b) logarithmic scale.

Conclusions

In this dissertation a new processing architecture to detect and track humans beyond walls has been introduced. In particular two different measurement methods have been developed and tested on experimental data.

A new method for through the wall detection and tracking of moving targets by means of radio-frequency imaging has been implemented. The method is capable of facing the two-dimensional tracking problem in terms of an inverse scattering one. The measurement algorithm is inherently tailored to real time applications. Once defined both the measurement configuration and geometry of the investigation domain, the SVD of the linear integral operator, which relates the measured scattered field and target positions and is characterized by a high computational burden, can in fact be off-line evaluated.

Several numerical and experimental tests have been carried out in order to assess the performance of the method. The tests have involved different geometrical models, number of moving targets, investigation domains and noise conditions. In all the considered configurations, the method has been capable of correctly reconstructing the trajectories of the considered targets. The differences between nominal and estimated positions of the target never greater than $0.18\ m$ have been encountered in both examples, corresponding to a relative accuracy of about *8%*, very close to that granted by [61].

Moreover, a very simple and effective method for detecting life signs in through-the-wall applications has been proposed and tested.

The method properly exploits a continuous wave signal source working at 10 GHz and takes advantage of the phase modulation due to the chest displacement in the respiratory movement to detect the respiratory activities from the measured signal. The proposed strategy allows the detection of life signs of people in furnished rooms behind concrete and brick walls.

Comparisons of the obtained results to those granted by other traditional techniques for Doppler frequency estimation highlighted the superior performance of the proposed method, in terms of available dynamic range and noise rejection. The proposed method allows extracting the required information on target frequency with an acquisition time significantly lower than that needed by the other techniques. Finally, remarkable advantages are obtained also in terms of computational burden; the adopted decorrelation strategy makes, in fact, the new method capable of providing its results in few seconds, with a significant reduction with respect to the other considered methods.

At the present, anyway, the proposed methods can be very interesting for USAR missions, in particular the vital signs detection method could be very useful in the case of trapped victims buried under rubble in the cavities created by collapsed building material after an earthquake. For this reason, in the near future new measurement campaigns are planned in USAR test-bed of the fire brigade of Pisa.

Bibliography

[1] D. D. Ferris, J. N. C. Currie, "A survey of current technologies for through-the-wall surveillance (TWS)", in *Proc. of SPIE Conference on Sensors, Information, and Training Technologies for Law Enforcement*, Boston, MA, 1998,Vol.3577, pp.62-72.

[2] C. A. Miles, "Through-the-Wall Surveillance: A New Technology for Saving Lives".

[3] Victor M. Lubecke, Olga Boric-Lubecke, Anders Host-Madsen, and Aly E. Fathy, "Through-the-Wall Radar Life Detection and Monitoring", in *Proc. of IEEE Microwave Symposium, Honolulu*, 2007, pp. 769-772.

[4] Q. Zhou, J. Liu, A. Host-Madsen, 0. Boric-Lubecke, and V. Lubecke, "Detection of Multiple Heartbeats Using Doppler Radar", in *Proc. of IEEE ICASSP*, 2006, vol.2, pp.12-18.

[5] N. Maaref, P. Millot, Ch. Pichot and O. Picon, "A Study of UWB FM-CW Radar for the Detection of Human Beings in Motion Inside a Building", *IEEE Trans. on Geosci. and Remote Sens.*, 47, (5), 2009, 1297-1300.

[6] M. Amin and K. Sarabandi, "Special issue on 'Remote sensing of the building interior'," *IEEE Trans. Geosci. Remote Sens.*, vol. 47, no. 5, pp. 1267–1268, May 2009.

[7] L. P. Song, C. Yu, and Q. H. Liu, "Through-wall imaging (TWI) by radar: 2-D tomographic results and analyses," *IEEE Trans. Geosci. Remote Sens.*, vol. 43, no. 12, pp. 2793–2798, Dec. 2005.

[8] S. S. Ram and H. Ling, “Through-wall tracking of human movers using joint Doppler and array processing,” *IEEE Geosci. Remote Sens. Lett.*, vol. 5, no. 3, pp. 537–541, Jul. 2008.

[9] M. Bertero and P. Boccacci, "Introduction to Inverse Problems in Imaging", U.K.: Inst. Phys., Bristol, 1998.

[10] J. B. Keller, “Inverse Problems”, Am. Math. Monthly, 83: 107-118, 1976.

[11] F. Soldovieri and R. Solimene, “Through-Wall Imaging via a Linear Inverse Scattering Algorithm”, *IEEE Geosci. Remote Sens. Lett.*, vol. 4, no. 4, October 2007.

[12] A. R. Hunt, “Image formation through walls using a distributed radar sensor array,” *in Proc. 32nd IEEE AIPR Workshop*, 2003, pp. 232–237.

[13] A. M. Attiya, A. Bayram, A. Safaai-Jazi, and S. M. Riad, “UWB applications for through-wall detection,” in *Proc. IEEE Antennas Propag*. Soc. Int. Symp., 2004, pp. 3079–3082.

[14] F. Aryanfar and K. Sarabandi, “Through wall imaging at microwave frequencies using space-time focusing,” in *Proc. IEEE Antennas Propag. Soc. Int. Symp*., 2004, pp. 3063–3066.

[15] Y. Yang and A. E. Fathy, “See-through-wall imaging using ultra wideband short-pulse radar system,” in *Proc. IEEE Antennas Propag. Soc.* Int. Symp., 2005, pp. 334–337.

[16] Hong Wang, Ram M. Narayanan, and Zheng Ou Zhou, “Through-Wall Imaging of Moving Targets Using UWB Random Noise Radar”, *IEEE Antennas and Wireless Propagation Letters*, Vol. 8, 2009.

[17] Kenneth E. Browne, Robert J. Burkholder and John L. Volakis, “Through-Wall Opportunistic Sensing System Utilizing a Low-Cost Flat-Panel Array”, *IEEE Transactions on Antennas and Propagation*, Vol. 59, 2011.

[18] A. Muqaibel, A. Safaai-Jazi, A. Bayram, A. M. Attiya, and S. M. Riad, "Ultra wideband through-the-wall propagation", in *Proc. Inst. Elect. Eng. — Microw.*, Antennas,Propag., Dec. 2005,vol. 152,pp.581–588.

[19] L. M. Brekhovskikh, "Waves in Layered Media", New York: Academic, 1960. (English translation byD. Lieberman).

[20] Y. Yamaguchi, Y. Maruyama, A. Kawakami, M. Sengoko, and T. Abe, "Detection of objects buried in wet snowpack by an FM-CW radar", *IEEE Trans. Geosci. Remote Sens.*, vol. 29,no. 2,pp. 201–208,Mar. 1991.

[21] F. Abujarad, A. Jostingmeier, and A. S. Omar, "Clutter removal for land mine using different signal processing techniques", *in Proc. 10th Int.Conf. Ground Penetrating Radar*, Delft, The Netherlands, Jun. 21–24, 2004, pp.697–700.

[22] P. Millot, N. Maaref, G. Autret, C. Pichot, J-Y. Dauvignac, and O. Picon, "New concepts for through the wall radar using multiple UWB antennas", in *Proc. IASTED Int. Conf. Antennas, Radar Wave Propag.*, Montreal, QC, Canada, May 30–Jun. 1, 2007, pp.126–131.

[23] F. Ahmad, Y. Zhang, and M. G. Amin, "Three-dimensional wideband beamforming for imaging through a single wall," *IEEE Geosci. Remote Sens. Lett.*, vol. 5,no. 2,pp. 176–179,Apr. 2008.

[24] Yinan Yu, Jian Yang, Tomas McKelvey, and Borys Stoew, "A Compact UWB Indoor and Through-Wall Radar with Precise Ranging and Tracking", *International Journal of Antennas and Propagation*, vol. 2012.

[25] Wenji Zhang, Moeness G. Amin, Fauzia Ahmad, Ahmad Hoorfar, and Graeme E. Smith, "Ultrawideband Impulse Radar Through-the-Wall Imaging with Compressive Sensing ", *International Journal of Antennas and Propagation*, vol. 2012.

[26] Muhammed Duman and Ali Cafer Gurbuz, "Performance Analysis of Compressive-Sensing-Based Through-the-Wall Imaging with Effect of

Unknown Parameters", *International Journal of Antennas and Propagation*, vol. 2012.

[27] F. Soldovieri, R. Solimene, and F. Ahmad, "Sparse Tomographic Inverse Scattering Approach for Through-the-Wall Radar Imaging", *IEEE Trans. on Instrum. Meas.*

[28] Kun-Mu, Yong Huang, Jianping Zhang and Adam Norman, "Microwave Life-Detection Systems for Searching Human Subjects Under Earthquake Rubble or Behind Barrier", *IEEE Transaction on Biomedical Engineering*, vol. 27, No.1, January 2000.

[29] A. D. Droitcour, O. Boric-Lubecke, V. M. Lubecke, J. Lin, G. T. A. Kovacs, "Range correlation and I/Q performance benefits in single-chip silicon Doppler radars for non-contact cardiopulmonary Monitoring", *IEEE Transactions on Microwave Theory and Techniques*, vol.52, No.3, pp. 838-847, March 2004.

[30] Y. Xiao, J. Lin, O. Boric-Lubecke, V. M. Lubecke, "A Ka-band low power Doppler radar system for remote detection of cardiopulmonary motion", Proceedings of the 2005 I*EEE Engineering in Medicine and Biology 27th Annual Conference*, Shanghai, China, September 1-4, 2005.

[31] C. Li, Y. Xiao, J. Lin, "Experiment and spectral analysis of a low-power Ka-band heartbeat detector measuring from four sides of a human body", *IEEE Transactions on Microwave Theory and Techniques*, vol.54, No.12, pp. 4464-4471, December 2006.

[32] Webster's New World™ Medical Dictionary, 3rd Edition, Wiley Publishing, May 2008.

[33] William D. McArdle,Frank I. Katch,Victor L. Katch, "Essentials of exercise physiology", Volume 1.

[34] M. D'Urso, G. Leone, F. Soldovieri, "A simple strategy for life signs detection via an X-band experimental set-up", *PIER Journal*, Progress in Electromagnetic Research Journal, 2009.

[35] Y. Xiao, J. Lin, O. Boric-Lubecke, V. M. Lubecke, "Frequency-Tuning Technique for Remote Detection of Heartbeat and Respiration Using Low-Power Double-Sideband Transmission in the Ka-Band", *IEEE Transactions on Microwave Theory and Techniques*, vol.54, No.5, May 2006.

[36] Changzhi Li and Jenshan Lin, "Random Body Movement Cancellation in Doppler Radar Vital Sign Detection", *IEEE Transactions on Microwave Theory and Techniques*, vol.56, No.12, December 2008.

[37] Jiang Long, Changzhan Gu, Yong Tao, Jiangtao Huangfu, S. Qiao, W. Z. Cui, W. Ma, Lixin Ran, "A novel direct-conversion structure for non-contact vital sign detection system", *8th International Symposium on Antenna, Propagation and EM Theory*, ISAPE 2008.

[38] Changzhi Li and Jenshan Lin, "Optimal Carrier Frequency of Non-contact Vital Sign Detectors", 2007 *IEEE Radio and Wireless Symposium*, pp. 281 – 284, 2007.

[39] M.Ascione, A.Buonanno, M.D'Urso, L.Angrisani, R.Schiano Lo Moriello, "Distributed sensing in homeland security applications", *Proceedings of IEEE International Workshop on Measurements and Networking*, October 10-11, 2011, Anacapri, Italy.

[40] Tian Jin, Bo Chen, and Zhimin Zhou, " Image-Domain Estimation of Wall Parameters for Autofocusing of Through-the-Wall SAR Imagery", *IEEE Trans. Geosci. Remote Sensing*.

[41] R. Solimene, F. Soldovieri, G. Prisco, and R. Pierri, "3D microwave tomography by a 2D slice based reconstruction algorithm", *IEEE Geoscience And Remote Sensing Letters*, 4, (4), (2007), pp. 556-560.

[42] A. Buonanno, M. D'Urso, G. Prisco, M. Felaco, L. Angrisani, M. Ascione, R. Schiano Lo Moriello, N. Pasquino, "A New Measurement Method for Through-The-Wall Detection and Tracking of Moving Targets", *Measurement 46,* pp. 1834–1848, Feb. 2013.

[43] F. Soldovieri and R. Solimene, "Through-wall imaging via a linear inverse scattering algorithm," *IEEE Geosci. Remote Sens. Lett.*, vol. 4, no. 4, pp. 513–517, Oct. 2007.

[44] L. P. Song, C. Yu, and Q. H. Liu, "Through-wall imaging (TWI) by radar: 2-D tomographic results and analyses," *IEEE Trans. Geosci. Remote Sens*., vol. 43, no. 12, pp. 2793–2798, Dec. 2005.

[45] R. Pierri, R. Solimene, A. Liseno, and J. Romano, "Linear Distribution Imaging of Thin Metallic Cylinders Under Mutual Scattering*", IEEE Trans. on Antennas and Propagation*, vol. 53, no. 9, September 2005.

[46] A. Brancaccio, C. Di Dio, G. Leone, "An algorithm for localization of cylinders by reflection mode scattered field*", Advances in Geosciences*, 19, (2008), pp.11-16.

[47] R. Solimene, F. Soldovieri, G. Prisco, and R. Pierri, "3D microwave tomography by a 2D slice based reconstruction algorithm", *IEEE Geoscience And Remote Sensing Letters,* 4, (4), (2007), pp. 556-560.

[48] R. Persico, F. Soldovieri, and G. Leone, "A microwave tomographic imaging approach for multibistatic configuration: The choice of the frequency step", *IEEE Trans. on Instrum. Meas*., 55, (6), (2006) pp. 1926-1934.

[49] M.Ascione, A.Buonanno, M.D'Urso, L.Angrisani, R.Schiano Lo Moriello, "Distributed sensing in homeland security applications", *Proceedings of IEEE International Workshop on Measurements and Networking*, October 10-11, 2011, Anacapri, Italy.

[50] M. Ascione, A. Buonanno, M. D'Urso, L. Angrisani R. Schiano Lo Moriello, "A New Measurement Method based on Music Algorithm for Through-the-Wall Detection of Life Signs", *IEEE Transactions on Instrumentation and Measurement*, Jan 2013, vol.62, N.1, pp.13-26.

[51] Byung-Kwon Park, Olga Boric-Lubecke and Victor M. Lubecke, "Arctangent Demodulation With DC Offset Compensation in Quadrature Doppler Radar Receiver Systems", *IEEE Transactions on Microwave Theory and Techniques*, vol.55, No.5, May 2007.

[52] R.O.Schmidt, "Multiple emitter location and signal parameter estimation," *IEEE Transactions on Antennas and Propagation*, vol. AP-34, pp.276-280, March 1986.

[53] Tong Li, Yinhui Tang, "Frequency Estimation based on Modulation FFTand MUSIC Algorithm", *First International Conference on Pervasive Computing, Signal Processing and Applications*, 2010.

[54] Jiang Yi, "Research on Harmonic Frequency Estimation Based on Non-parameter Methods" Cheng Du: University of Electronic Science and Technology of China, 2008.

[55] M. F. Fahmy and Y. M. Y. Hasan, "Signal de-noising using Hankel matrix rank reduction", *2lSt National Radio Science Conference* (NRSC2004), March 16-18, 2004.

[56] H. Akaike,"Information Theory and an extension of the maximum likelihood principle," in *Proc. 2nd Inter.Symposium on Information Theory*, Budapest, 1973, pp. 267-281.

[57] I. Kopriva, W. Wasylkiwskyj,"Estimating number of sub-Gaussian emitters in a narrowband DOA estimation problem by using independent component analysis," in *Proc. of Antennas and Propagation*, July 3-8, 2005, pp. 97-100.

[58] P. Stoica, and R. Moses, Introduction to Spectral Analysis, Upper Saddle River, NJ: Prentice Hall, 1997.

[59] Yee K. S., Numerical Solution of Initial Boundary Value Problems Involving Maxwell's Equations in Isotropic Media, *IEEE Transactions on Antennas*, 1966.

[60] Currie, N.C., Ferris, D.D., and al, "New Law Enforcement Applications Of Millimeter Wave Radar", *SPIE*, Vol. 3066, pp2-10, 1997.

[61] Yinan Yu, Jian Yang, Tomas McKelvey, and Borys Stoew, "A Compact UWB Indoor and Through-Wall Radar with Precise Ranging and Tracking", *International Journal of Antennas and Propagation*, vol. 2012.